

# 1 Crustal structure of southeast Australia from teleseismic 2 receiver functions

3 Mohammed Bello<sup>1,2</sup>, David G. Cornwell<sup>1</sup>, Nicholas Rawlinson<sup>3</sup>, Anya M. Reading<sup>4</sup>, Othaniel  
4 K. Likkason<sup>2</sup>

5 <sup>1</sup>Department Geology & Geophysics, University of Aberdeen, Aberdeen, UK

6 <sup>2</sup>Department of Physics, Abubakar Tafawa Balewa University, Bauchi, Nigeria

7 <sup>3</sup>Department of Earth Sciences, University of Cambridge, UK

8 <sup>4</sup>School of Natural Sciences (Physics), University of Tasmania, Australia

9 *Correspondence to:* Nicholas Rawlinson (nr441@cam.ac.uk)

10 **Abstract.** In an effort to improve our understanding of the seismic character of the crust beneath southeast  
11 Australia, and how it relates to the tectonic evolution of the region, we analyse teleseismic earthquakes recorded  
12 by 24 temporary and 8 permanent broadband stations using the receiver function method. Due to the proximity  
13 of the temporary stations to Bass Strait, only 13 of these stations yielded usable receiver functions, whereas  
14 seven permanent stations produced receiver functions for subsequent analysis. Crustal thickness, bulk seismic  
15 velocity properties and internal crustal structure of the southern Tasmanides – an assemblage of Palaeozoic  
16 accretionary orogens that occupy eastern Australia – are constrained by H- $\kappa$  stacking and receiver function  
17 inversion, which point to: (1) a ~39.0 km thick crust, an intermediate-high  $V_p/V_s$  ratio (~1.70-1.76), relative to  
18 ak135, and a broad (>10 km) crust-mantle transition beneath the Lachlan Fold Belt. These results are interpreted  
19 to represent magmatic underplating of mafic materials at the base of the crust; (2) a complex crustal structure  
20 beneath VanDieland, a putative Precambrian continental fragment embedded in the southernmost Tasmanides,  
21 which features strong variability in crustal thickness (23-37 km) and  $V_p/V_s$  ratio (1.65-1.93), the latter of which  
22 likely represents compositional variability and the presence of melt. The complex origins of VanDieland, which  
23 comprises multiple continental ribbons, coupled with recent failed rifting and intraplate volcanism, likely  
24 contributes to these observations; and (3) stations located in the East Tasmania Terrane and Eastern Bass Strait  
25 (ETT+EB) collectively indicate crust of uniform thickness (31-32 km), which clearly distinguish it from  
26 VanDieland to the west. Moho depths are also compared with the continent-wide AusMoho model in southeast  
27 Australia, and are shown to be largely consistent, except in regions where AusMoho has few constraints (e.g.  
28 Flinders Island). A joint interpretation of the new results with ambient noise, teleseismic tomography and  
29 teleseismic shear wave splitting anisotropy, helps provide new insight into the way that the crust has been  
30 shaped by recent events, including failed rifting during the break-up of Australia and Antarctica and recent  
31 intraplate volcanism.

32 **Keywords:** receiver functions, crustal structure, VanDieland, Bass Strait, SE Australia

## 33 1 Introduction

34 The Phanerozoic Tasmanides (Collins and Vernon, 1994; Coney, 1995; Coney et al., 1990) comprise the eastern  
35 one-third of the Australian continent and through a process of subduction accretion were juxtaposed against the  
36 eastern flank of the Precambrian shield region of Australia beginning in the Late Neoproterozoic and Early  
37 Palaeozoic (Foster and Gray, 2000; Glen, 2005; Glen et al., 2009; Moresi et al., 2014) (Figure 1). Persistent

38 sources of debate that impede a more complete understanding of the geology of the Tasmanides include: (1) the  
39 geological link between Tasmania – an island state in southeast Australia – and mainland Australia, which are  
40 separated by the waters of Bass Strait; and (2) the presence and locations of continental fragments from  
41 Rodinian remnants that are entrained within the accretionary orogens. Furthermore, the lateral boundaries  
42 between individual tectonic blocks and their crustal structure are often not well defined. To date, few constraints  
43 on crustal thickness and seismic velocity structure have been available for regions such as Bass Strait.  
44 Constraints on the Moho transition, crustal thickness and velocity structure beneath Bass Strait derived from  
45 receiver functions (RFs) can therefore provide fresh insight into the nature and evolution of the Tasmanides.

46 Previous estimates of crustal thickness and structure beneath southeastern Australia have been obtained from  
47 deep seismic reflection transects, wide-angle seismic data, topography and gravity anomalies (e.g. Collins,  
48 1991; Collins et al., 2003; Drummond et al., 2006 and Kennett et al., 2011). Earlier RF studies in southeast  
49 Australia (Shibutani et al., 1996; Clitheroe et al., 2000; Tkalčić et al., 2011; Fontaine et al., 2013a,b) suggested  
50 the presence of complex lateral velocity variations in the mid-lower crust that probably reflect the interaction of  
51 igneous underplating, associated thinning of the lithosphere, recent hotspot volcanism and uplift. Furthermore,  
52 the intermediate to high crustal  $V_p/V_s$  ratio of 1.70–1.78 in this region (Fontaine et al., 2013a), relative to  
53 continental crust where  $V_p/V_s$  is  $\sim 1.68$ , may indicate a mafic composition that includes mafic granulite rocks,  
54 granite-gneiss and biotite gneiss. Body- and surface-wave tomography (Fishwick and Rawlinson, 2012;  
55 Rawlinson et al., 2015) revealed  $P$  and  $S$  wave velocity anomalies in the uppermost mantle beneath Bass Strait  
56 and the Lachlan Fold Belt. Ambient noise surface wave tomography (Bodin et al., 2012b; Young et al., 2012;  
57 Pilia et al., 2015b, 2016; Crowder et al., 2019) of the southern Tasmanides revealed significant crustal  
58 complexity, but is unable to constrain crustal thickness or the nature of the Moho transition.

59 The goal of this paper is to provide fresh insight into the crust and Moho structure beneath the southern  
60 Tasmanides using  $P$ -wave RFs and explain the origin of the lateral heterogeneities that are observed. This will  
61 allow us to explore the geological relationship between the different tectonic units that constitute the southern  
62 Tasmanides, and develop an improved understanding of the region's tectonic history.

## 63 **2 Geological setting**

64 The Palaeozoic-Mesozoic Tasmanides of eastern Australia form part of one of the most extensive accretionary  
65 orogens in existence and evolved from interaction between the East Gondwana margin and the Proto-Pacific  
66 Ocean. The tectonic evolution of the Tasmanides is complex and large-scale reconstructions have proven  
67 difficult. This is evident from the variety of models that have been suggested to explain how the region formed  
68 (Foster and Gray, 2000; Spaggiari et al., 2003; Teasdale et al., 2003; Spaggiari et al., 2004; Boger and Miller,  
69 2004; Glen, 2005; Cawood, 2005; Glen et al., 2009; Cayley, 2011a,b; Gibson et al., 2011; Moresi et al., 2014;  
70 Pilia et al., 2015a,b). Particular challenges arise from multiple subduction events, multiple phases of  
71 metamorphism, entrainment of exotic continental blocks, the formation of large oroclinal, recent intraplate  
72 volcanism and subsequent events, including the separation of Antarctica and Australia and the formation of the  
73 Tasman Sea. These challenges are compounded by the presence of widespread sedimentary sequences that  
74 hinder direct access to basement rocks (Fig. 1).

75 The Tasmanides consist of four orogenic belts, namely the Delamerian, Lachlan, Thomson and New England  
76 Orogens. The Delamerian Orogen - located in the south - is the oldest part of the Tasmanides and has a  
77 southward extension across Bass Strait from Victoria into western Tasmania, where it is commonly referred to  
78 as the Tyennan Orogen (Berry et al., 2008). Between about 514 and 490 Ma, the Precambrian and Early  
79 Cambrian rocks that constitute the Delamerian Orogen were subjected to a contractional orogenic event along  
80 the margin of East Gondwana (Foden et al., 2006). Subsequently, the Lachlan Orogen formed in the east, which  
81 contains rocks that vary in age from Ordovician to Carboniferous (Glen, 2005). Gray and Foster (2004) argued  
82 for a tectonic model of the Lachlan Orogen that involved interaction of a volcanic arc, oceanic microplates and  
83 three distinct subduction zones. Each subduction zone is linked to the formation of a distinct tectonic terrain: the  
84 Stawell-Bendigo zone, Tabbarebbera zone and Narooma accretionary complex. The limited rock exposure in the  
85 Tasmanides as a whole has made direct observation of the Lachlan Orogen difficult; this is attributed to a large  
86 swath of Mesozoic-Cenozoic sedimentary cover and more recent Quaternary volcanics, which obscure a large  
87 portion of the underlying Palaeozoic terrane. However, the Lachlan Orogen contains belts of Cambrian rocks in  
88 Victoria and New South Wales that are similar in age to the Delamerian Orogen (Gray and Foster, 2004).

89 The presence of Precambrian outcrops in Tasmania and the relative lack of similar age rocks in adjacent  
90 mainland Australia has led to different models which attempted to explain the existence of Proterozoic  
91 Tasmania. For instance, Li et al. (1997) suggested that western Tasmania may be the remnant of a continental  
92 fragment set adrift by Rodianian break-up, whereas Calvert and Walter (2000) proposed that King Island, along  
93 with western Tasmania, rifted away from the Australian craton around ~600 Ma (Fig. 1). Other researchers have  
94 developed scenarios in which the island of Tasmania was present as a separate microcontinental block that was  
95 positioned outboard of the eastern margin of Gondwana before re-attaching at the commencement of the  
96 Palaeozoic (Berry et al., 2008).

97 A popular model that attempts to reconcile the geology observed in Tasmania and adjacent mainland Australia  
98 is that of Cayley (2011a). This model proposes that central Victoria and western Tasmania formed a  
99 microcontinental block called "VanDieland" that fused with East Gondwana at the end of the Cambrian,  
100 possibly terminating the Delamerian Orogeny. VanDieland became entangled in the subduction-accretion  
101 system which built the Palaeozoic orogens that now comprise eastern Australia (Fig. 1). Delineating  
102 Precambrian continental fragments within southeast Australia has proven difficult, partly due to more recent  
103 sedimentary cover that obscures large tracts of the Tasmanides. However, if present, they likely have distinctive  
104 structural and seismic velocity characteristics (Glen, 2013).

### 105 **3 Previous geophysical studies**

106 A variety of geophysical methods have so far been employed to study the crustal structure of the Tasmanides.  
107 Shibutani et al. (1996) applied a non-linear inversion method to RF waveforms to constrain the shear wave  
108 velocity beneath broadband seismic stations in eastern Australia. They found that the Moho is relatively shallow  
109 (30-36 km depth) and sharp within the cratonic region, and deeper (38-44 km) and transitional along the axis of  
110 the Tasmanides. They suggested that crustal thickening of the fold belt by underplating or intrusion of mantle  
111 materials may have contributed to this observation. Clitheroe et al. (2000) built on this earlier work by inverting  
112 RFs to map broad-scale crustal thickness and Moho character across the Australian continent. They found that in

113 general, there was good agreement between xenolith-derived estimates of Moho depth and those determined by  
114 RF inversion, except beneath the Lachlan Fold Belt, where a broad Moho transition may be present. Overall,  
115 however, the RF results were consistent with those determined by Drummond and Collins (1986) and Collins  
116 (1991), who used seismic reflection and refraction transects to determine that the Lachlan Fold Belt includes the  
117 thickest crust ( $\sim 50$  km) in eastern Australia. A more recent study by Fontaine et al. (2013a) employed  $H$ - $\kappa$   
118 stacking and non-linear RF inversion to investigate crustal thickness, shear wave velocity structure, as well as  
119 dipping and anisotropy of the crustal layers. Their results also indicated a thick crust ( $\sim 48$  km) and an  
120 intermediate (2-9 km) crust-mantle transition beneath the Lachlan Fold Belt, which could be attributed to  
121 underplating beneath the crust and/or high concentrations of mafic rocks in the mid-lower crust. Their results  
122 also showed a dipping Moho together with crustal anisotropy in the vicinity of three seismic stations (YNG,  
123 CNB and CAN).

124 Over the last decade, ambient noise tomography has become a popular tool for studying the structure of the  
125 Australian crust. Saygin and Kennett (2010) produced the first group velocity maps of the Australian continent  
126 from Rayleigh wave group velocity dispersion in the period range 5.0–12.5 seconds. Limited spatial resolution  
127 ( $\sim 2^\circ \times 2^\circ$ ) in our study region means that this model is only able to represent the structure beneath Bass Strait as  
128 a broad, low velocity anomaly. However, the group velocities exhibit a good correlation with known basins and  
129 cratons. Subsequent studies using denser arrays covering southeast mainland Australia (Arroucau et al., 2010),  
130 southeastern Australia (Young et al. 2013), and northern Tasmania (Young et al., 2011) show good correlations  
131 between group/phase velocity maps and sedimentary and basement terrane boundaries. In order to account for  
132 uneven data distribution, Bodin et al. (2012b) used a Bayesian transdimensional inversion scheme to generate  
133 group velocity maps that span the Australian continent from multi-scale ambient noise datasets. However, in our  
134 study area their model is of low resolution due to the limited station coverage and hence few details on crustal  
135 structure can be inferred. Bodin et al. (2012a) subsequently applied Bayesian statistics to reconstruct the Moho  
136 geometry of Australia using a variety of seismic datasets, which gave an approximate Moho depth of  $\sim 30$  km  
137 beneath Bass Strait. Pilia et al. (2015a,b) and Crowder et al. (2019) derived 3-D shear wave velocity models of  
138 the Bass strait region using ambient noise data from the same array of temporary stations that we exploit in this  
139 study. They were able to constrain the lateral and depth extent of the primary sedimentary basins in the region,  
140 and provide insight into the seismic character of the Precambrian micro-continental block that appears to  
141 underpin southern Victoria, north western Tasmania and Bass Strait.

142 Teleseismic tomography has also been used to image the lithosphere beneath southeast Australia, thanks in part  
143 to the prolific deployment of short-period seismometers as part of the WOMBAT transportable array project  
144 (Rawlinson and Kennett, 2008, Rawlinson et al., 2015, 2016). While the main focus has been on the upper  
145 mantle, in Tasmania, where station spacing was denser, some constraints on crustal velocity structure were  
146 possible. Rawlinson et al. (2006) found that the crust beneath the ETT was significantly faster than the crust  
147 beneath central Tasmania, which may represent a contrast between crust with oceanic provenance in the east and  
148 Precambrian continental provenance in the west. Bello et al. (2019b) built on this work by including teleseismic  
149 arrival time data from the same temporary deployment as the the current study to generate a detailed upper  
150 mantle model of southeast Australia, which revealed that Bass Strait was underlain by lower velocities,  
151 consistent with thinned lithosphere as a result of failed rifting during the break-up of Australia and Antarctica.

152 Active source seismic profiling has also been widely used in southeast Australia to characterize crustal velocity  
153 structure (e.g. Finlayson et al., 1980; Collins, 1991; Finlayson et al., 2002; Drummond et al., 2006; Glen, 2013).  
154 This has largely focused on the transition from continental to oceanic crust at passive margins, but has also been  
155 used to image major transition zones or faults between orogens (Glen, 2013) or within orogens (Cayley et al.,  
156 2011a,b), the latter of which lead to the VanDieland microcontinental model. Rawlinson and Urvoy (2006)  
157 jointly inverted teleseismic arrival times and active source wide-angle traveltimes in northern Tasmania to  
158 constrain crustal velocity, Moho geometry and upper mantle velocity structure and found that both northeastern  
159 and northwestern Tasmania is characterised by thinner (<28 km) and higher velocity crust compared to central  
160 Tasmania.

161 Potential field data have also been exploited to study the formation and structure of the Tasmanides. Gunn et al.  
162 (1997) integrated potential field data (magnetic and gravity), seismic reflection data, outcrop geology and well  
163 information to study the crustal structure of the Australian continent. Their study found that the occurrence of  
164 tensional stress, oriented NE-SW along basement structures in the Bass Basin, is able to explain the formation of  
165 the three major sedimentary basins that overlie dense mafic material, which in turn was formed by mantle  
166 decompression processes associated with crustal stretching. From the interpretation of new aeromagnetic data,  
167 Morse et al. (2009) delineated the architecture of the Bass Strait basins and their supporting basement structure.  
168 Subsequent studies by Moore et al. (2015, 2016) used gravity, magnetic, seismic reflection and outcrop data to  
169 support the hypothesis of a VanDieland microcontinent. Their study showed that VanDieland comprises seven  
170 distinct microcontinental ribbon terranes that appear to have amalgamated by the Late Cambrian, with major  
171 faults and suture zones bonding these ribbon terranes together.

172 While the last few decades have seen important advances and insights made into our understanding of the  
173 southern Tasmanides, there still remains limited data on the deep crustal structure beneath Bass Strait, which is  
174 our region of interest. It is therefore timely that we can exploit, using the RF technique, teleseismic data  
175 recorded by a collection of temporary and permanent seismic stations in the region to study the structure of the  
176 crust, Moho and uppermost mantle beneath mainland Australia, Bass Strait and Tasmania.

#### 177 **4 Data**

178 A collaboration involving five organisations (University of Tasmania, Australian National University, Mineral  
179 Resources Tasmania, the Geological Survey of Victoria and FROGTECH) deployed the temporary Bass seismic  
180 array from May 2011 to April 2013. It consisted of 24 broadband, three-component seismic stations that  
181 spanned northern Tasmania, and a selection of islands in Bass Strait and southern Victoria. The instruments  
182 used were 23 Güralp 40T and one Güralp 3ESP sensors coupled to Earth Data PR6-24 data loggers. The  
183 permanent stations consist of eight broadband sensors managed by IRIS, GEOSCOPE and the Australian  
184 National Seismic Network (ANSN). The distribution of all 32 seismic stations that are used in this study is  
185 plotted in Figure 2. Earthquakes with magnitudes  $m_b > 5.5$  at epicentral distances between  $30^\circ$  and  $90^\circ$  comprise  
186 the seismic sources used in this analysis (Fig. 3). This resulted in an acceptable azimuthal coverage of  
187 earthquakes between the northwest and east of the array, where active convergence of the Australian and  
188 Eurasian plate coupled with westward motion of the Pacific plate has produced extensive subduction zones. To  
189 the south and southwest of the array, the absence of subduction zones in the required epicentral distance range

190 means that there are significantly fewer events available for analysis from these regions.

## 191 **5 Methods**

### 192 **5.1 Receiver functions**

193 The RF technique (Langston, 1979) uses earthquakes at teleseismic distances to enable estimation of Moho  
194 depth and shear wave velocity structure in the vicinity of a seismic recorder. If this technique can be applied to a  
195 network of stations with good spatial coverage, it represents an effective way of mapping lateral variations in  
196 Moho depth and crustal structure.

197 A recorded teleseismic wavefield at a broadband station can be described by the convolutional model in which  
198 operators that represent the source radiation pattern, path effects, crustal structure below the station and  
199 instrument response are combined to describe the recorded waveform. By using deconvolution to remove the  
200 effects of the source, path and response of the instrument (e.g. Langston, 1979), information on local crustal  
201 structure beneath the station can be extracted from *P-S* wave conversions at discontinuities in seismic velocity  
202 (Owens et al., 1987; Ammon, 1991).

203 *P*-wave RFs were determined from teleseismic *P*-waveforms using FuncLab software (Eagar and Fouch, 2012;  
204 Porritt and Miller, 2018), following preprocessing using the seismic analysis code (SAC) (Goldstein et al.,  
205 2003). RFs were computed by applying an iterative time-domain deconvolution scheme developed by Ligorria  
206 and Ammon (1999) with a 2.5 s Gaussian filter width. This is achieved by deconvolution of the vertical  
207 component waveform from the radial and transverse waveforms with a central frequency of  $\sim 1$  Hz. This  
208 frequency was selected on account of significant source energy detected in the  $\sim 1$  Hz range of teleseismic *P*  
209 arrivals, which are sensitive to crustal-scale anomalies. It also provides a favourable lateral sensitivity with  
210 respect to Fresnel zone width ( $\sim 15$  km at Moho depth) when the conversions from *P* to *S* are mapped as  
211 velocity and crustal thickness variations.

212 The complete set of 1765 events (Fig. 3) and 32 stations produced 21,671 preliminary RFs. These RFs were  
213 manually inspected using the FuncLab trace editor and a subset of 9,674 RFs were selected for further analysis  
214 using the visual clarity of the direct arrivals as an acceptance criterion. Due to high noise levels and fewer  
215 events associated with the temporary BASS array dataset, a modest number of good quality RFs resulted from  
216 the above selection method, so different selection criteria were applied that assessed the *P*-arrival, Moho  
217 conversion and later amplitudes in conjunction with overall noise levels exhibited by the transverse component  
218 RFs. This enabled the temporary BASS stations to yield between 2 and 30 good quality receiver functions, and  
219 increased the number of stations where H- $\kappa$  stacking and NA inversion could be applied from 13 to 20.

### 220 **5.2 H- $\kappa$ stacking**

221 Having obtained reliable *P*-wave RFs, the *H- $\kappa$*  stacking technique is used to estimate crustal thickness and bulk  
222  $V_p/V_s$  for individual stations. We apply the method of Zhu and Kanamori (2000) to stations where the direct *P*  
223 (Moho *P*-to-*S* conversion) phase and its multiples are observed. This technique makes use of a grid search to  
224 determine the crustal thickness (*H*) and  $V_p/V_s$  ( $\kappa$ ) values that correspond to the peak amplitude of the stacked

225 phases. A clear maximum requires a contribution from both the primary phase ( $P_s$ ) and the associated multiples  
 226 ( $PpPs$  and  $PpSs+PsPs$ ). In the absence of multiples, the maximum becomes smeared out due to the inherent  
 227 trade-off between crustal thickness ( $H$ ) and average crustal velocity properties ( $\kappa$ ) (Ammon et al., 1990; Zhu and  
 228 Kanamori, 2000). The  $H$ - $\kappa$  stacking algorithm reduces the aforementioned ambiguity by summing RF  
 229 amplitudes for  $P_s$  and its multiples -  $PpPs$  and  $PpSs+PsPs$  - at arrival times corresponding to a range of  $H$  and  
 230  $V_p/V_s$  values. In the  $H$ - $\kappa$  domain the equation for stacking amplitude is

$$231 \quad s(H, \kappa) = \sum_{j=1}^N w_1 r_j(t_1) + w_2 r_j(t_2) + w_3 r_j(t_3) \quad (1)$$

232 where  $r_j(t_i)$ ;  $i=1,2,3$  are the RF amplitude values at the expected arrival times  $t_1$ ,  $t_2$ ,  $t_3$  of the  $P_s$ ,  $PpPs$ ,  
 233  $PpSs+PsPs$  phases respectively for the  $j^{\text{th}}$  RF,  $w_1$ ,  $w_2$ ,  $w_3$  are weights based on the signal to noise ratio  
 234 ( $w_1+w_2+w_3=1$ ), and  $N$  is the total number of radial RFs for the station.  $s(H, \kappa)$  achieves its maximum value when  
 235 all three phases stack constructively, thereby producing estimates for  $H$  and  $V_p/V_s$  beneath the station (see  
 236 Figure 5 and Supplementary Figures S1-S4). In this study, the weighting factors used are  $w_1=0.6$ ,  $w_2=0.3$ ,  
 237  $w_3=0.1$ . The  $H$ - $\kappa$  approach requires an estimate of the mean crustal  $P$ -wave velocity, which is used as an initial  
 238 value. Based on the results of a previous seismic refraction study (Drummond and Collins, 1986), we use an  
 239 average crustal velocity of  $V_p = 6.65$  km/s to obtain our estimates of  $H$  and  $\kappa$  in the study area, noting that  $H$ - $\kappa$   
 240 stacking results are much more dependent on  $V_p/V_s$  than  $V_p$  (Zhu and Kanamori, 2000). To estimate the  
 241 uncertainties in the  $H$ - $\kappa$  stacking results, we compute the standard deviation of the  $H$  and  $\kappa$  values at each  
 242 station. When only a small number of RFs are available at a station (e.g. 4 in the case of MILA) the estimates  
 243 are unlikely to be particularly robust, and in such instances are perhaps best viewed as a lower bounds on  
 244 uncertainty.

245 While simple to implement, the Zhu and Kanamori (2000) method can suffer from large uncertainties due to its  
 246 assumption of a simple flat-laying layer over a half-space with constant crustal and upper mantle properties.  
 247 Consequently, there are only two search parameters ( $H$  and  $\kappa$ ) plus *a priori* information ( $V_p$ , weightings) and it  
 248 does not account for variation with backazimuth. These problems can cause non-unique and inaccurate  
 249 estimates, which can lead to potentially misleading interpretations; for instance, a low velocity upper crustal  
 250 layer can appear as a very shallow Moho in an  $H$ - $\kappa$  stacking search space diagram. Also, a dipping Moho and/or  
 251 anisotropic layers within the crust can contribute to uncertainty.

### 252 **5.3 Nonlinear waveform inversion**

253 In an effort to refine the crustal model, we invert a stack of the radial RFs by adopting the workflow described  
 254 by Shibutani et al. (1996). We divide the waveform data (RFs) into four 90° quadrants based on the backazimuth  
 255 of their incoming energy. The 1<sup>st</sup> quadrant backazimuth range is from 0° and 90°, and an equivalent range in a  
 256 clockwise direction defines the consecutive quadrants. The 2<sup>nd</sup> and 3<sup>rd</sup> quadrants (south-eastern and south-  
 257 western backazimuths) have very small numbers of RFs. Data from the 1<sup>st</sup> and 4<sup>th</sup> quadrants are of better quality,  
 258 with the 1<sup>st</sup> quadrant showing more coherency than the 4<sup>th</sup> quadrant, which is likely due to the orientation of  
 259 surrounding tectonic plate boundaries and hence the pattern of  $P$ -wave energy radiated towards Australia.

260 Kennett and Furumura (2008) showed that seismic waves arriving in Australia from the northern azimuths  
 261 undergo multiple scattering but low intrinsic attenuation due to heterogeneity in the lower crust and mantle; this  
 262 tends to produce prolonged high-frequency coda. An important assumption in our inversion is that we neglect  
 263 anisotropy and possible Moho dip, which we assume have a second order influence on the waveforms we use to  
 264 constrain 1-D models of the crust and upper mantle.

265 Visual examination of coherency in  $P$  to  $S$  conversions allows us to select a subset of RF waveforms for  
 266 subsequent stacking. This resulted in groups of mutually coherent waveforms after which a moveout correction  
 267 is then applied to remove the kinematic effect of different earthquake distances prior to stacking using a cross-  
 268 correlation matrix approach described in Chen et al. (2010) and Tkalčić et al. (2011). Our visual acceptance  
 269 criteria yields RFs at only 14 out of the 32 stations used for this study. An example of some stacked RFs is  
 270 given in Figure 4.

271 We invert RFs for 1-D seismic velocity structure beneath selected seismic stations using the Neighbourhood  
 272 Algorithm or NA (Sambridge, 1999a,b) in order to better understand the internal structure of the crust and the  
 273 nature of the transition to the upper mantle. NA makes use of Voronoi cells to help construct a searchable  
 274 parameter space, with the aim of preferentially sampling regions of low data misfit. In the inversion process, a  
 275 Thomson-Haskell matrix method (Thomson, 1950 and Haskell, 1953) was used to calculate a synthetic radial  
 276 RF for a given 1-D (layered) structure. During the inversion, as in Shibutani et al. (1996) and Clitheroe et al.  
 277 (2000), each model is described by six layers: a layer of sediment, a basement layer, an upper crust, middle crust  
 278 and lower crust, and an underlying mantle layer, all of which feature velocity gradients and potentially, velocity  
 279 jumps across boundaries. The inversion involves constraining 24 parameters:  $V_s$  values at the top and bottom of  
 280 each layer, layer thickness and the  $V_p/V_s$  ratio in each layer (Table 1). The inclusion of  $V_p/V_s$  ratio as an  
 281 unknown primarily aims to accommodate the effects of a sediment layer with limited prior constraints  
 282 (Bannister et al., 2003). There are two important controlling parameters required by NA: (1) the number of  
 283 models produced per iteration ( $n_s$ ); and (2) the number of neighbourhoods re-sampled per iteration ( $n_r$ ). After a  
 284 number of trials we chose the maximum number of iterations to be 5500, with  $n_s=13$  and  $n_r=13$  for all iterations.  
 285 We employ a chi-squared  $\chi^2$  metric (see Sambridge 1999a for more details) to compute the misfit function,  
 286 which is a measure of the inconsistency between the true  $\phi_i^{obs}$ , and predicted,  $\phi_i^{pre}(m)$  waveforms for a  
 287 given model  $m$ :

$$288 \quad \chi_v^2(m) = \frac{1}{v} \sum_{i=1}^{N_d} \left( \frac{\phi_i^{obs} - \phi_i^{pre}(m)}{\sigma_i} \right)^2 \quad (2)$$

289 where  $\sigma_i$  represents the noise standard deviation determined from  $\phi_i^{obs}$ , following the method described in  
 290 Gouveia and Scales (1998), and  $v$  represents the number of degrees of freedom (the difference between the  
 291 number of observations and the number of parameters being inverted for). Using the above stated parameters,  
 292 the inversion targets the 1-D structure that produces the best fit between the predicted and observed RF. Figures

293 7-9 and Supplementary Figures S5-S8 present example results of inversions via density plots of the best 1000  
294 data-fitting  $S$ -wave velocity models produced by the NA. The optimum data fitting model is plotted in red. Note  
295 that receiver function inversion was limited to fitting the waveform between 0 and 30 seconds after the P-arrival  
296 for temporary BASS network stations because this produced superior results to the -5 – 30 second time window  
297 used for permanent station data.

## 298 **6 Results**

### 299 **6.1 $H$ - $\kappa$ stacking results**

300 Maps of crustal thicknesses and average  $V_p/V_s$  from  $H$ - $\kappa$  stacking in southeast Australia from 16 stations are  
301 shown in Figure 6. At the remaining stations, we could not detect any clear multiples or Moho conversions in  
302 the RFs from any direction. A previous study by Chevrot and van der Hilst (2000) has noted that this region is  
303 devoid of clear multiples. The crustal thickness for all analysed stations in the study area varies from  $23.2 \pm 5.0$   
304 km (BA02) beneath NW Tasmania to  $39.1 \pm 0.5$  km (CAN) beneath the Lachlan Fold Belt, and the variation  
305 strongly correlates with topography. Crust beneath VanDieland (Fig. 6a) is thin in the north ( $\sim 37.5$  km) and  
306 south ( $\sim 33$  km), but appears to be considerably thinner beneath the Victorian and Tasmanian margin of Bass  
307 Strait ( $\sim 25$  km). The mountainous region of the Lachlan Fold Belt has the deepest Moho at  $39.1 \pm 0.5$  km  
308 (CAN) and a corresponding  $V_p/V_s$  value of  $1.73 \pm 0.02$ . Crust that is consistently between  $\sim 31$  and 33 km thick  
309 lies beneath the East Tasmania Terrane and Eastern Bass Strait (ETT+EB).  $V_p/V_s$  ratio varies between  $\sim 1.65$   
310 beneath station BA11, which also exhibits the thinnest crust, and  $\sim 1.93$  beneath stations BA19 and BA20 in  
311 southern Victoria. There is no obvious correlation between the number of RFs used in the  $H$ - $\kappa$  stacking and the  
312 size of the uncertainty in either Moho depth or  $V_p/V_s$ , but as mentioned previously, the uncertainty estimates  
313 for stations with a low number of RFs are likely to be less robust. Table 2 shows a summary of  $H$ - $\kappa$  stacking  
314 results for the stations that have been analysed.

### 315 **6.2 Nonlinear inversion results**

316 Results of the NA inversion were successfully obtained for a selection of permanent and temporary stations, as  
317 shown in Table 2 and Figure 10. If the Moho is defined by a gentle velocity gradient, the base of the velocity  
318 gradient is used as a proxy for the Moho depth, as done in previous RF (e.g. Clitheroe et al., 2000; Fontaine et  
319 al., 2013a) and seismic refraction (Collins, 1991; Collins et al., 2003) studies. We also adopt an upper mantle  
320 velocity of  $V_p = 7.6$  km/s (i.e.  $V_s = 4.3$ - $4.4$  km/s for  $V_p/V_s$  ratios of 1.73-1.77 at the base of the Moho gradient)  
321 following Clitheroe et al. (2000) who used this value for RF studies, and Collins et al. (2003) who used  $V_p > 7.8$   
322 km/s for their summary of both seismic refraction and RF results; these  $V_p$  values are consistent with global  
323 Earth models (e.g. Kennett et al., 1995). Therefore, we also require the  $S$ -wave velocity to be  $> \sim 4.4$  km/s  
324 beneath the Moho. We present the  $S$ -wave velocity profiles from the NA inversion for stations CAN, MOO,  
325 TOO, YNG, BA13 and BA17 in Figures 7-9, together with observed and predicted RFs. The  $S$ -wave velocity  
326 inversion results of the remaining stations are included as supplementary material (see Supplementary Figures  
327 S5-S8). In assigning the Moho depth, we consider three criteria to examine the quality of the inversion result:  
328 (1) misfit value  $\chi^2$ ; (2) the quality of the RF stack (which is based on our ability to pick the direct and multiple  
329 phases); and (3) the visual fit between the synthetic and observed RF. Models that fail to fit significant arrivals

330 in the observed RF are rejected. Based on these criteria, the inversion results are classified as:

- 331 • Very good: very low  $\chi^2$  (typically  $< 0.4$ ), very good visual fit to direct and multiple phases.
- 332 • Good: low  $\chi^2$  (typically 0.4-0.8), direct phases clearly visible, multiple phases less clear, and a good  
333 visual fit to all major identifiable phases.
- 334 • Poor: medium to high  $\chi^2$  (in the range 0.8-1.2), direct phases visible, multiple phases unclear, and  
335 moderate visual fit to some identifiable phases.

336 In general, the optimum  $\chi^2$  value is normally considered to be 1, since below this value, the tendency is to fit  
337 noise rather than signal. However, this is for the ideal case when the number of degrees of freedom and the  
338 absolute values of the data uncertainty are well known (e.g. in the case of a synthetic test). In the case of  
339 observational data, these values are often poorly constrained, so using the relative  $\chi^2$  values coupled with visual  
340 assessment of the data fit appears to be reasonable. With regard to the character of the crust-mantle transition,  
341 this study classifies the transition zone as sharp  $\leq 2$  km, intermediate 2-10 km or broad  $\geq 10$  km as initially  
342 proposed by Shibutani et al. (1996) and modified by Clitheroe et al. (2000).

343 We note that for the seven permanent stations for which we produce receiver function inversion/H- $\kappa$  stacking  
344 results, five have estimates of Moho depth from previous receiver function studies. Clitheroe et al., (2000)  
345 estimated Moho depth at 49 km beneath CAN based on a non-linear inversion, which is  $\sim 10$  km greater than the  
346 results we obtain for both NA inversion and H- $\kappa$  stacking (see section 7.1 for further discussion of this  
347 discrepancy). Ford et al. (2010) determine Moho depth beneath stations MOO, TOO, TAU and YNG using H- $\kappa$   
348 stacking and find values (compared to our H- $\kappa$  stacking results) of  $33 \pm 3$  km ( $33.0 \pm 1.2$  km),  $34 \pm 3$  km ( $37.5 \pm 1.2$   
349 km),  $32 \pm 3$  km ( $33.5 \pm 1.9$  km) and  $33 \pm 2$  km ( $37.3 \pm 0.5$  km) respectively. These are all within error, with the slight  
350 exception of station YNG, located in Young, on the western flanks of the Great Dividing Range, where we  
351 might expect the crust to be slightly thicker than average. Overall, however, these similarities suggest that our  
352 results are likely to be robust.

## 353 **7 Discussion**

354 For convenience, the seismic stations are separated into three groups (Fig. 2) based on tectonic setting and the  
355 results obtained. Stations YNG, CAN, CNB, MILA and BA13 are located in the Lachlan Fold Belt; stations  
356 BA02, BA11, BA19, BA20, TAU, MOO and TOO sit above the VanDieland microcontinental block; and  
357 stations BA07, BA08, BA09 and BA17 lie in the East Tasmania Terrane and Eastern Bass Strait (ETT+EB).  
358 Stations BA22 and BA24 lie to the west of VanDieland. This discussion focuses on crustal thickness, the nature  
359 of the Moho and crustal velocity and velocity ratio variations from H- $\kappa$  stacking and the 1-D S-wave velocity  
360 models. Overall, the agreement between Moho depths obtained from the H- $\kappa$  stacking results and NA-inversion  
361 is generally within error (Table 2), which makes a joint interpretation more straight forward. Comparison is also  
362 made to other studies that have examined crustal seismic properties in southeast Australia, and we attempt to  
363 integrate our new findings with previous results from teleseismic tomography, SKS splitting and ambient noise  
364 tomography in order to better understand the crust and upper mantle structure and dynamics beneath this region.

## 365 7.1 Lateral variation of crustal thickness and nature of the Moho

366 The RF analysis clearly reveals the presence of lateral changes in crustal thickness that span mainland Australia  
367 through Bass Strait to Tasmania (Figures 6 and 10; in the latter case, RF depths from previous studies are also  
368 included for reference). The stations located in the Palaeozoic Lachlan Fold Belt reveal a generally thick crust  
369 that ranges between ~37 and 40 km. Although the Moho was picked as a velocity jump for stations YNG, CAN  
370 and CNB, the velocity nonetheless tends to continue to increase with depth below the discontinuity. This,  
371 coupled with the fact that Clitheroe et al. (2000) estimate the Moho to be almost 10 km deeper beneath CAN, is  
372 consistent with the presence of mafic underplating (e.g. Drummond and Collins, 1986; Shibutani et al., 1996;  
373 Clitheroe et al., 2000), sourced from the ambient convecting mantle. The top and bottom of such a layer could  
374 feature a velocity step with depth and its internal structure is likely to be layered and/or gradational, hence  
375 resulting in uncertainty in the true Moho depth. Based on deep crustal reflection profiling, Glen et al. (2002)  
376 suggested that the deep Moho underlying the Lachlan Orogen results from magmatic underplating that added a  
377 thick Ordovician mafic layer at the base of the crust coupled with a thick sequence of Ordovician mafic rocks  
378 that can be found in the mid and lower crust. Finlayson et al. (2002) and Glen et al. (2002) also inferred the  
379 presence of underplating near CNB and CAN from seismic refraction data. Collins (2002) postulated that the  
380 underplating might have occurred in the back-arc region of a subduction zone due to pronounced adiabatic  
381 decompression melting in the asthenosphere. The seismic tomography model of Rawlinson et al. (2010, 2011)  
382 exhibits an increase in *P*-wavespeed at 50 km depth beneath CAN, CNB and YNG and the authors suggest that  
383 magmatic underplating may be the cause of the high velocity anomaly. A recent study by Davies et al. (2015)  
384 identified the longest continental hotspot track in the world (over 2000 km total length), which began in north  
385 Queensland at ~33 Ma, and propagated southward underneath the present-day Lachlan Fold Belt and Bass  
386 Strait. The magmatic underplating could therefore be a consequence of the passage of the continent above a  
387 mantle upwelling leading to a more diffuse crust-mantle transition zone. The thickened crust and a transitional  
388 Moho observed in the Lachlan Fold Belt are consistent with the proposed delamination models of Collins and  
389 Vernon (1994).

390 Strong lateral changes in crustal seismic structure (Figures 6 and 10) beneath VanDieland appear to be a  
391 reflection of the region's complex tectonic history. The thick crust (~37 km) beneath the Selwyn Block (see  
392 Figure 1 for its location) – within the northern margin of VanDieland in southern Victoria – thins dramatically  
393 to ~26 km as it enters Bass Strait, increases to ~30 km beneath King Island (BA11), then thins to ~23 km  
394 beneath NW Tasmania, before increasing to ~33 km in southern Tasmania. The results in southern Tasmania  
395 agree with those of Korsch et al. (2002) from a seismic reflection profile adjacent to the seismic stations TAU  
396 and MOO. The thinner crust beneath Bass Strait and its margins may be a consequence of lithospheric thinning  
397 and/or delamination associated with failed rifting that accompanied the break-up of Australia and Antarctica  
398 (Gaina et al., 1998). Stations BA07, BA08, BA09 and BA17 (ETT+EB) collectively indicate crust of relative  
399 uniform thickness (~31-32 km, Figures 10a,b). Relative to western Bass Strait, the crust is slightly thicker in  
400 this part of the study area, which may suggest underplating associated with a Palaeozoic subduction system (e.g.  
401 Drummond and Collins, 1986; Gray and Foster, 2004).

402 In general, our understanding of crustal thickness variations are limited by station separation, so it is difficult to

403 determine whether smooth variations in thickness or step-like transitions explain the observations.

## 404 7.2 $V_p/V_s$ and bulk crustal composition

405  $V_p/V_s$  can constrain chemical composition and mineralogy more robustly than  $P$ - or  $S$ -wave velocity in isolation  
406 (Christensen and Fountain, 1975). We observe variations in  $V_p/V_s$  across the study region, which we can largely  
407 equate with variations in composition or melt. Studies in mineral physics and field observations show (1) an  
408 increase in  $V_p/V_s$  with decreasing  $\text{SiO}_2$  content in the continental crust (Christensen, 1996) and (2) partial melt  
409 is revealed by elevated  $V_p/V_s$ , especially if the anomaly is localised to an intra-crustal layer (Owens and Zandt,  
410 1997). A more felsic ( $\text{SiO}_2$ ) composition in the lower crust is represented by a lower  $V_p/V_s$ , which reflects  
411 removal of an intermediate-mafic zone by delamination, whereas a more mafic lower crust is revealed by higher  
412  $V_p/V_s$  ( $> 1.75$ ) which may be due to underplated material (Pan and Niu, 2011). However, lower crustal  
413 delamination can also result in decompression melting, which can yield elevated  $V_p/V_s$  (He et al., 2015). We  
414 interpret the variation of observed  $V_p/V_s$  in the southern Tasmanides to be a consequence of compositionally  
415 heterogeneous crust and localised partial melt that may likely be sourced from recent intraplate volcanism  
416 (Rawlinson et al., 2017).

417 Figure 6b shows the distribution of bulk  $V_p/V_s$  across the study area. The pattern of  $V_p/V_s$  ratios appears to  
418 delineate three distinct zones of crust. Beneath the Lachlan Orogen, values are  $\sim 1.75$ , which is consistent with  
419 the presence of a mafic lower crust, as suggested by a number of other studies (Drummond and Collins, 1986;  
420 Shibutani et al., 1996; Clitheroe et al., 2000; Finlayson et al., 2002). Beneath eastern Bass Strait, the  $V_p/V_s$   
421 ratios are slightly lower, with BA07, BA08 and BA09 exhibiting values of 1.70, 1.70 and 1.71 respectively.  
422 These values are in agreement with constraints from seismic reflection and refraction studies (Finlayson et al.,  
423 2002; Collins et al., 2003) and may indicate a felsic to intermediate crustal composition. The geology of  
424 Flinders Island, which hosts both BA07 and BA08, is dominated by Devonian granites, which is consistent with  
425 this observation. Beneath VanDieland,  $V_p/V_s$  is highly variable, with the greatest contrast between BA11  
426 ( $\sim 1.65$ ) and BA19/20 ( $\sim 1.93$ ), and BA19/20 and TOO (1.68). BA11 is located on King Island, which is  
427 characterised by Precambrian and Devonian granite outcrops, which may help explain the low  $V_p/V_s$ . The high  
428  $V_p/V_s$  beneath BA19/20 is harder to explain, but could be caused by melt in the crust associated with the Newer  
429 Volcanics Province, which sits along the Cosgrove intraplate volcanic track, and last erupted only  $\sim 4.6$  ka  
430 (Rawlinson et al., 2017). The return to lower  $V_p/V_s$  beneath TOO over a relatively short distance ( $\sim 100$  km) is  
431 also difficult to explain, but we note that this region of Victoria is underlain by granite intrusions.

432 In summary, the crust beneath VanDieland exhibits the greatest lateral heterogeneity in  $V_p/V_s$ , which likely  
433 reflects considerable variations in composition and the presence of melt. This can partially be explained by the  
434 tectonic history of the region, which includes failed rifting in Bass Strait accompanied by widespread magma  
435 intrusion and granite emplacement, and more recently, the passage of a plume (Rawlinson et al., 2017).  
436 Furthermore, Moore et al. (2015) used reflection transects and potential field data to infer that VanDieland is  
437 comprised of up to seven continental ribbon terranes that are bounded by major faults and suture zones, which  
438 were likely amalgamated by the end of the Proterozoic. Hence, considerable variations in composition and  
439 hence  $V_p/V_s$  ratio are to be expected.

### 440 7.3 Moho depth comparison

441 Prior to this study, a variety of seismic methods have been used to constrain Moho depth in southeast Australia,  
442 including receiver functions, reflection profiling and wide-angle reflection and refraction experiments. In an  
443 effort to combine the results from all of these studies into a single synthesis, Kennett et al., (2011) developed the  
444 AusMoho model. This included Moho depth estimates from over 11,000 km of reflection transects across the  
445 continent, numerous refraction studies, and 150 portable and temporary stations. Due to irregular sampling, the  
446 detail of this model is highly variable; for example, the region beneath Bass Strait is constrained by only five  
447 measurements, whereas the central Lachlan Fold Belt around Canberra (see Figure 1 for location) features  
448 relatively dense sampling at ~50 km intervals or less.

449 AusMoho includes previous receiver function results from Shibutani et al. (1996), Clitheroe et al. (2000),  
450 Fontaine et al. (2013a) and Tkalcic et al (2012), as well as reflection and refraction transects in Tasmania, parts  
451 of the Lachlan Orogen, and western Victoria. Figure 11 illustrates AusMoho for our study region, which  
452 exhibits large variations in Moho depth (from ~10 km to >50 km). These extremes are due to the presence of  
453 oceanic crust outboard of the passive margin of the Australian continent, and the root beneath the Southern  
454 Highlands, which represent the southern extension of the Great Dividing Range in New South Wales.  
455 Superimposed on Figure 11 are Moho depths from the four previous receiver function studies cited above, plus  
456 NA inversion and H- $\kappa$  depth estimates from this study. As expected, the correlation between the previous RF  
457 results and AusMoho is generally good, since they were part of the dataset used to build this model. In places  
458 where they don't match, this can be attributed to the presence of seismic refraction or reflection lines which  
459 were also used to constrain AusMoho.

460 In general, the agreement between the results from this study and AusMoho is good, but there are exceptions.  
461 For instance, CAN, CNB, YNG and MILA tend to be somewhat shallower than AusMoho. However, this can be  
462 attributed to the likely presence of mafic underplating alluded to earlier, which can effectively yield two options  
463 for the Moho transition due to an expected high ( $>1.85$ )  $V_p/V_s$  in the underplate layer (e.g. Cornwell et al.,  
464 2010). AusMoho Moho depths beneath BA07 and BA08 are considerably shallower than our estimates, which  
465 we attribute to a lack of data coverage in this region. Sizeable discrepancies also exist beneath BA02, BA19 and  
466 BA20; in the former case, the uncertainty in our H- $\kappa$  stacking estimate is 5 km, which may be a factor here. In  
467 the latter case, we also note that there is sparse data coverage southeast of Melbourne to constrain AusMoho, so  
468 it would appear that our new Moho depths are more likely to be correct. Overall, while there is good consistency  
469 between AusMoho and our new results, any updated version of AusMoho should incorporate the Moho depth  
470 estimates from this study.

471 Although AusMoho did make use of results from a 3-D wide-angle reflection and refraction survey of Tasmania  
472 (offshore shots and on-shore stations), it only used a few sample points for the final Moho model (Kennett et al.,  
473 2011), and therefore the resolution of AusMoho is considerably less than the Moho model produced by  
474 Rawlinson et al. (2001). Consequently, we plot our three RF results on top of this model in Supplementary  
475 Figure S9. The agreement between the Moho model and RF depths beneath MOO and TAU is good, but RF  
476 estimates beneath BA02 are shallower than the Moho model by about 4 km. However, this is within the margin  
477 of error for the H- $\kappa$  stacking result.

## 478 7.4 Synthesis

479 In this final section, we present a synthesis of results for southeast Australia that are based on: (1) our new  
480 receiver function results; (2) teleseismic SKS splitting results from Bello et al. (2019a); (3) teleseismic  
481 tomography undertaken by Bello et al. (2019b); (4) ambient noise crustal imaging results from Young et al.  
482 (2013); and (5) AusMoho (Kennett et al., 2011). This synthesis is encapsulated in the plot shown in Figure 12,  
483 which is a representative transect through the Lachlan Orogen south through Bass Strait and into Tasmania.  
484 Moho depths are taken from AusMoho, and refined where additional information is available from our new RF  
485 results; crustal P-wave velocity is taken from the ambient noise results (following conversion from *S*-wave  
486 velocity – see Bello et al, 2019b for more details); and mantle *P*-wave velocities are taken from Bello et al,  
487 (2019b). Arrows are based on interpreted mantle flow patterns undertaken as part of the shear wave splitting  
488 study. This previous study used approximately the same temporary and broadband station network that was used  
489 in the current study, and found that beneath the Lachlan Orogen, fast axis orientations of anisotropy were  
490 aligned with contemporary plate motion (NNE), but beneath Bass Strait, a radial pattern was observed that is  
491 consistent with an upwelling mantle that impinges on the lithosphere and spreads out in all directions.  
492 Interestingly, the location of this phenomenon corresponds approximately to the predicted location of the  
493 Cosgrove hotspot track source (Davies et al., 2015), and may be caused by an upwelling mantle plume. Thus,  
494 the low velocities in the upper mantle beneath Bass Strait may be due to elevated temperatures and melt,  
495 although it is not straightforward to explain the higher velocities below 200 km depth in this context.

496 The thicker Moho boundary beneath the Lachlan Orogen (Figure 12) reflects the likely presence of  
497 underplating, which makes the base of the crust harder to discern seismically. However, the crust is clearly  
498 thicker here than beneath Bass Strait or Tasmania. Moho depth beneath the northern part of the Figure 12 is not  
499 constrained by our RF results, but according to AusMoho, it is relatively flat, which is consistent with  
500 Precambrian crust, and there is a faster mantle lithosphere. The strong variations in crustal velocity beneath Bass  
501 Strait can be attributed to failed rifting resulting in the formation of thick (>10 km) sedimentary basins and  
502 elevated temperatures (lower velocities), and intrusion of mafic rich material into the lower and mid crust  
503 (higher velocities).

## 504 8 Conclusions

505 We used *H-κ* stacking of teleseismic RFs to determine crustal thickness and  $V_p/V_s$  ratio and generate 1-D *S*-  
506 wave velocity profiles of the crust from RF inversion in order to investigate the internal crustal velocity  
507 structure beneath the southern Tasmanides in southeast Australia. Our main findings are summarised below.

- 508 • The thick crust and broad crust-mantle transition beneath the Lachlan Fold Belt may be caused by  
509 magmatic underplating of mafic materials beneath the crust, which is consistent with an elevated  $V_p/V_s$   
510 ratio (relative to ak135) of  $\sim 1.73$ . Thicker crust is also to be expected from the elevated topography of  
511 the eastern Lachlan Fold Belt.
- 512 • The crustal structure is complex beneath VanDieland. It thins considerably from the northern tip of the  
513 microcontinent ( $\sim 37$  km) into Bass Strait ( $\sim 26$  km) and northern Tasmania ( $\sim 23$  km), yet in southern

514 Tasmania the crust is somewhat thicker (~33 km) compared to Bass Strait. This may in part be due to  
515 the complex origins of the microcontinent, which appears to be comprised of multiple Precambrian  
516 continental ribbons, but is also likely due to failed rifting in Bass Strait before and during the  
517 separation of Australia and Antarctica. This resulted in lithospheric stretching/delamination, magmatic  
518 intrusion, and the deposition of thick sedimentary sequences. Recent intraplate volcanism and the  
519 possible progression of a mantle plume beneath VanDieland in the last few thousand years may also  
520 have produced compositional heterogeneity and melt in the crust. Such events are likely to contribute  
521 significantly to variations in crustal thickness and the pronounced changes in  $V_p/V_s$  that we observe.

522 • Stations within the ETT+EB collectively indicate crust of uniform thickness (~31-32 km) and uniform  
523  $V_p/V_s$  (~1.70), which clearly distinguishes it from VanDieland. This region of the crust likely  
524 represents a southern continuation of the Lachlan Orogen, and therefore is underpinned by crust of  
525 oceanic origin.

526 • Comparison of our new Moho depth results with the AusMoho model reveals an overall consistency,  
527 although at some of our station locations where AusMoho has few constraints, there are noticeable  
528 differences, such as southern Victoria and beneath Flinders Island. The discrepancies beneath the  
529 Lachlan Orogen are attributed to the presence of underplated mafic material, which can obfuscate the  
530 location of the Moho.

531 • A synthesis of our new RF results with pre-existing teleseismic tomography, shear wave splitting and  
532 ambient noise studies reveals a complex lithosphere that has clearly been impacted by orogeny  
533 (thickened crust), failed rifting beneath Bass Strait (thinned crust and complex crustal velocities), and  
534 recent intraplate volcanism (high  $V_p/V_s$  ratios and a radial pattern of fast anisotropy patterns above a  
535 presumed zone of mantle upwelling).

536

## 537 **9 Data availability**

538 Dataset available at [10.6084/m9.figshare.12233723](https://doi.org/10.6084/m9.figshare.12233723)

539

## 540 **10 Author contributions**

541 M.B. performed the data analysis and wrote the draft manuscript. N.R and D.C. guided the study and assisted in  
542 interpretation. M.B., D.C. and N.R. discussed the results and revised the manuscript. A.R. and O.L. revised the  
543 manuscript and assisted with the interpretation.

544 **11 Competing Interests:** The authors declare no competing interests.

## 545 **12 Acknowledgments**

546 The work in this paper was performed as part of a PhD study and has been jointly funded by Abubakar Tafawa  
547 Balewa University (ATBU), Bauchi, Nigeria and the University of Aberdeen, UK. The authors acknowledge the  
548 efforts of staff, students and fieldwork technicians from the Australian National University and University of  
549 Tasmania, who deployed the temporary BASS array used in this study. We also thank Qi Li and Armando  
550 Arcidiaco for their efforts in BASS data pre-processing and archiving. Australian Research Council Grant  
551 LP110100256 supported the BASS deployment. We are grateful to IRIS and Geoscience Australia for providing  
552 data from several stations in mainland Australia and Tasmania. Figure 1 was made using Inkscape software  
553 (Harrington, et. al., 2005) and Figures 2, 3, 6 and 9 were produced using the Generic Mapping Tools (Wessel et  
554 al., 2013).

555

## 556 **References**

557 Amante, C. and Eakins, B. W.: ETOPO1 1 Arc-Minute Global Relief Model: Procedures, data sources and  
558 analysis, NOAA technical memorandum NESDIS NGDC-24, 19pp, 2009.

559 Ammon, C. J.: The isolation of receiver effects from teleseismic P waveforms. *Bull. Seis. Soc. Ame.*, 81, 2504–  
560 2510, 1991.

561 Ammon, C. J., Randall, G., and Zandt, G.: On the nonuniqueness of receiver function inversions. *J. Geophys.*  
562 *Res.*, 95, 15 303–15 318, 1990.

563 Arroucau, P., Rawlinson, N., and Sambridge, M.: New insight into Cainozoic sedimentary basins and  
564 Palaeozoic suture zones in southeast Australia from ambient noise surface wave tomography. *Geophys. Res.*  
565 *Lett.*, 37, <http://dx.doi.org/10.1029/2009GL041974>, 2010.

566 Bannister, S., Yu, J., Leitner, B., and Kennett, B. L. N.: Variations in crustal structure across the transition from  
567 West to East Antarctica, Southern Victoria Land, *Geophys. J. Int.*, 155, 870–884, 2003.

568 Bello, M., Cornwell, D. G., Rawlinson, N., and Reading, A. M.: Insights into the structure and dynamics of the  
569 upper mantle beneath Bass Strait, southeast Australia, using shear wave splitting, *Phys. Earth Planet. Inter.*,  
570 289, 45–62, <https://doi.org/10.1016/j.pepi.2019.02.002>, 2019a.

571 Bello, M., Rawlinson, N., Cornwell, D. G., Crowder, E., Salmon, M., and Reading, A. M.: Structure of the crust  
572 and upper mantle beneath Bass Strait, southeast Australia, from teleseismic body wave tomography, *Phys.*  
573 *Earth Planet. Inter.*, 294, <https://doi.org/10.1016/j.pepi.2019.106276>, 2019b.

574 Berry, R. F., Steele, D. A., and Maffre, S.: Proterozoic metamorphism in Tasmania: implications for tectonic  
575 reconstructions, *Prec. Res.*, 166, 387–396. <https://doi.org/10.1016/j.precamres.2007.05.004>, 2008.

576 Bodin, T., Salmon, M., Kennett, B. L. N., and Sambridge, M.: Probabilistic surface reconstruction from multiple  
577 datasets: an example for the Australian Moho, *J. Geophys. Res.: Solid Earth*, 117,  
578 <http://dx.doi.org/10.1029/2012JB009547>, 2012a.

579 Bodin, T., Sambridge, M., Rawlinson, N., and Arroucau, P.: Transdimensional tomography with unknown data  
580 noise, *Geophys. J. Int.*, 189, 1536–1556, 2012b.

581 Boger, S. and Miller, J.: Terminal suturing of Gondwana and the onset of the Ross Delamerian Orogeny: the  
582 cause and effect of an Early Cambrian reconfiguration of plate motions, *Earth Planet. Sci. Lett.*, 219, 35–48,  
583 2004.

584 Calvert, C. R. and Walter, M. R.: The Late Neoproterozoic Grassy Group of King Island, Tasmania: correlation  
585 and palaeogeographic significance, *Precam. Res.*, 100, 299–312, 2000.

586 Cawood, P. A.: Terra Australis Orogen: Rodinia breakup and development of the Pacific and Iapetus margins of  
587 Gondwana during the Neoproterozoic and Palaeozoic. *Earth-Science Reviews*, 69, 249–279,

- 588 <http://dx.doi.org/10.1016/j.earscirev.2004.09.001>, 2005.
- 589 Cayley, R.: Exotic crustal block accretion to the eastern Gondwanaland margin in the Late Cambrian Tasmania,  
590 the Selwyn Block, and implications for the Cambrian–Silurian evolution of the Ross, Delamerian, and  
591 Lachlan orogens. *Gond. Res.*, 19, 628–649. <http://dx.doi.org/10.1016/j.gr.2010.11.013>, 2011a.
- 592 Cayley, R., Korsch, R. J., Moore, D. H., Costelloe, R. D., Nakamura, A., Willman, C. E., Rawlin, T. J., Morand,  
593 V. J., Skladzien, P. B., and O’Shea, P. J.: Crustal architecture of central Victoria: results from the 2006 deep  
594 crustal reflection seismic survey, *Aust. J. Earth Sci.*, 59, 113–156, 2011b.
- 595 Chen, Y., Niu, F., Liu, R., Huang, Z., Tkalčić, H., Sun, L., and Chan, W.: Crustal structure beneath China from  
596 receiver function analysis, *J. Geophys. Res.*, 49(B033067), 2010.
- 597 Chevrot, S. and van der Hilst, R. D.: The Poisson ratio of the Australian crust: Geological and Geophysical  
598 implications, *Earth Planet. Sci. Lett.*, 183,121–132, 2000.
- 599 Christensen, N. I.: Poisson’s ratio and crustal seismology, *J. Geophys. Res.*, 101, 3139–3156, 1996.
- 600 Christensen, N. I. and Fountain, D. M.: Constitution of the lower continental crust based on experimental studies  
601 of seismic velocities in granulite, *Geol. Soc. Ame. Bull.*, 86, 227–236, 1975.
- 602 Clitheroe, G., Gudmundsson, O., and Kennett, B.: The crustal thickness of Australia, *J. Geophys. Res.*, 105, 13  
603 697–13 713, 2000.
- 604 Collins, C. D. N.: The nature of crust–mantle boundary under Australia from seismic evidence, In: Drummond  
605 B. J. ed. *The Australian lithosphere*, *Geol. Soc. Aust. Spec. Pub.*, 17, 67–80, 1991.
- 606 Collins, C. D. N., Drummond, B. J., and Nicoll, M. G.: Crustal thickness patterns in the Australian continent,  
607 *Geol. Soc. Ame. Spec. Papers*, 372, 121–128, 2003.
- 608 Collins, W. J.: Nature of extensional accretionary origins, *Tectonics*, 21, 1024–1036, 2002.
- 609 Collins, W. J. and Vernon, R. H.: A rift–drift–delamination model of continental evolution: Palaeozoic tectonic  
610 development of eastern Australia, *Tectonophysics*, 2(35), 1994.
- 611 Coney, P. J.: Plate tectonics and the Precambrian Phanerozoic evolution of Australia, PACRIM ’95, *Aust. Inst.*  
612 *Mining and Metallurgy*, pages 145–150, 1995.
- 613 Coney, P. J., Edwards, A., Hine, R., Morrison, F., and Windrim, D.: The regional tectonics of the Tasman  
614 orogenic system, eastern Australia, *J. Struct. Geol.*, 12(5/6), 519–543, 1990.
- 615 Cornwell, D. G., P. K. H. Maguire, R. W. England, and G. W. Stuart (2010), Imaging detailed crustal structure  
616 and magmatic intrusion across the Ethiopian Rift using a dense linear broadband array, *Geochem. Geophys.*  
617 *Geosyst.*, 11, Q0AB03, doi:[10.1029/2009GC002637](https://doi.org/10.1029/2009GC002637).
- 618 Crowder, E., Rawlinson, N., Pilia, S., Cornwell, D. G., and Reading, A. M.: Transdimensional ambient noise  
619 tomography of Bass Strait, southeast Australia, reveals the sedimentary basin and deep crustal structure  
620 beneath a failed continental rift, *Geophys. J. Int.*, 217, 970–987, 2019.
- 621 Davies, D. R., Rawlinson, N., Iaffaldano, N., and Campbell, I. H.: Lithospheric controls on magma composition  
622 along Earth’s longest continental hotspot track, *Nature*, 525, 511–514, 2015.
- 623 Drummond, B. J. and Collins, C. D. N.: Seismic evidence for underplating of the lower continental crust of  
624 Australia, *Earth Planet. Sci. Lett.*, 79, 361–372, 1986.
- 625 Drummond, B. J., Lyons, P., Goleby, B., and Jones, L.: Constraining models of the tectonic setting of the giant  
626 Olympic Dam iron-oxide-copper-gold deposit, south Australia, using deep seismic reflection data,  
627 *Tectonophysics*, 420, 91–103, 2006.

- 628 Eagar, K. C. and Fouch, M. J.: FuncLab: A MATLAB interactive toolbox for handling receiver function  
629 datasets, *Seismo. Res. Lett.*, <https://doi.org/10.1785/gssrl.83.3.596>, 2012.
- 630 Finlayson, D. M., Collins, C. D. N., and Denham, D.: Crustal structure under the Lachlan Fold Belt,  
631 southeastern Australia, *Phys. Earth Planet. Int.*, 21, 321–342, 1980.
- 632 Finlayson, D. M., Korsch, R. J., Glen, R. A., Leven, J. H., and Johnstone, D. W.: Seismic imaging and crustal  
633 architecture across the Lachlan transverse zone, a crosscutting feature of eastern Australia, *Aust. J. Earth  
634 Sci.*, 49, 311–321, 2002.
- 635 Fishwick, S. and Rawlinson, N.: 3–D structure of the Australian lithosphere from evolving seismic datasets,  
636 *Aust. J. Earth Sci.*, 59, 809–826, 2012.
- 637 Foden, J., Elburg, M. A., Dougherty-Page, J., and Burt, A.: The timing and duration of the Delamerian  
638 Orogeny: correlation with the Ross Orogen and implications for Gondwana assembly, *J. Geology*, 114, 189–  
639 210, 2006.
- 640 Fontaine, F. R., Tkalčić, H., and Kennett, B. L. N.: Crustal complexity in the Lachlan Orogen revealed from  
641 teleseismic receiver functions, *Aust. J. Earth Sci.*, 60, 413–430, 2013a.
- 642 Fontaine, F. R., Tkalčić, H., and Kennett, B. L. N.: Imaging crustal structure variation across southeastern  
643 Australia, *Tectonophysics*, 582, 112–125, 2013b.
- 644 Foster, D. A. and Gray, D. R.: Evolution and structure of the Lachlan Fold Belt (Orogen) of eastern Australia,  
645 *Annu. Rev. Earth Planet. Sci.*, 28, 47–80, 2000.
- 646 Gaina, C., Müller, D., Royer, J. Y., Stock, J., Hardebeck, J., and Symonds, P.: The tectonic history of the  
647 Tasman Sea, a puzzle with 13 pieces, *J. Geophys. Res.*, 103, 12,413–12,433, 1998.
- 648 Gibson, G. M., Morse, M. P., Ireland, T. R., and Nayak, G. K.: Arc-continent collision and orogenesis in  
649 western Tasmanides: insights from reactivated basement structures and formation of an ocean-continent  
650 transform boundary off western Tasmania, *Gondwana Res.*, 19, 608–627, 2011.
- 651 Glen, R. A.: The Tasmanides of Eastern Australia. In: Vaughan, A. P. M., Leat, P. T., Pankhurst, R. J. (Eds.),  
652 *Terrane Processes at the Margins of Gondwana*, Geological Society, pages 23–96, 2005.
- 653 Glen, R. A.: Refining accretionary orogen models for the Tasmanides of eastern Australia, *Aust. J. Earth Sci.*,  
654 60, 315–370, 2013.
- 655 Glen, R. A., Korsch, R. J., Direen, N. G., Jones, L. E. A., Johnstone, D. W., Lawrie, K. C., Finlayson, D. M.,  
656 and Shaw, R. D.: Crustal structure of the Ordovician Macquarie Arc, eastern Lachlan Orogen, based on  
657 seismic–reflection profiling, *Aust. J. Earth Sci.*, 49, 323–348, 2002.
- 658 Glen, R. A., Percival, I. G., and Quinn, C. D.: Ordovician continental margin terranes in the Lachlan Orogen,  
659 Australia: implications for tectonics in an accretionary orogen along the east Gondwana margin, *Tectonics*,  
660 28, <https://doi.org/10.1029/2009TC002446>, 2009.
- 661 Goldstein, P., Dodge, D., Firpo, M., and Minner, L.: SAC2000: Signal processing and analysis tools for  
662 seismologists and engineers. Lee, W. H. K. and Kanamori, H. and Jennings, P. C. and Kisslinger, C. (Eds.).  
663 In *IASPEI International Handbook of Earthquake and Engineering Seismology*, Academic Press, London,  
664 2003.
- 665 Gouveia, W. P. and Scales, J. A.: Bayesian seismic waveform inversion: Parameter estimation and uncertainty  
666 analysis, *J. Geophys. Res.*, 103, 2759–2779, 1998.
- 667 Gray, D. R. and Foster, D. A.: Tectonic evolution of the Lachlan Orogen, southeastern Australia: historical  
668 review, data synthesis and modern perspectives, *Aust. J. Earth Sci.*, 51, 773– 817, 2004.
- 669 Gunn, P. J., Maidment, D. W., and Milligan, P.: Interpreting aeromagnetic data in areas of limited outcrop,

- 670 AGSO J. Aust. Geol. Geophys., 17, 175–185, 1997.
- 671 Harrington, B. et al (2004-2005). Inkscape. <http://www.inkscape.org/>.
- 672 Haskell, N. A.: The dispersion of surface waves in multilayered media, Bulletin of the Seismological Society  
673 America, 43, 1734, <http://dx.doi.org/10.1038/physci245109a0>, 1953.
- 674 He, C. S., Santosh, M., Dong, S. W., and Wang, S. C.: Crustal thickening and uplift of the Tibetan Plateau  
675 inferred from receiver function analysis, J. Asian Earth Sci., 99, 112–124, 2015.
- 676 Heintz, M. and Kennett, B. L. N.: Continental scale shear wave splitting analysis: Investigation of seismic  
677 anisotropy underneath the Australian continent, Earth Planet. Sci. Lett., 236, 106–119, 2005.
- 678 Kennett, B. L. N., Engdhal, E. R., and Buland, R.: Constraints on seismic velocities in the earth from travel  
679 times. Geophys. J. Int., 125, 228-248, 1995.
- 680 Kennett, B. L. N. and Furumura, T.: Stochastic waveguide in the lithosphere: Indonesian subduction zone to  
681 Australian craton, Geophys. J. Int., 172, 363–382, 2008.
- 682 Kennett, B. L. N., Salmon, M., Saygin, E., and Group, A.: AusMoho: the variation of Moho depth in Australia,  
683 Geophys. J. Int., 187, 946–958, 2011.
- 684 Korsch, R. J., Barton, T. J., Gray, D. R., Owen, A. J., and Foster, D. A.: Geological interpretation of a deep  
685 seismic reflection transect across the boundary between the Delamerian and Lachlan Orogens, in the vicinity  
686 of the Grampians, western Victoria, Aust. J. Earth Sci., 49, 1057–1075, <http://dx.doi.org/10.1046/j.1440-0952.2002.00963.x>, 2002.
- 688 Langston, C. A.: Structure under Mount Rainier, Washington, inferred from teleseismic body waves, J.  
689 Geophys. Res., 84, 4749–4762, <https://doi.org/10.1071/EG994019>, 1979.
- 690 Li, Z. X., Baillie, P. W., and Powell, C. M.: Relationship between northwestern Tasmania and East  
691 Gondwanaland in the Late Cambrian/Early Ordovician Paleomagnetic evidence, Tectonics, 16, 161–171,  
692 <http://dx.doi.org/10.1029/96TC02729>, 1997.
- 693 Ligorria, J. P. and Ammon, C. J.: Iterative deconvolution and receiver function estimation, Bull. Seism. Soc.  
694 Ame., 89, 1395–1400, 1999.
- 695 Moore, D., Betts, P. G., and Hall, M.: Fragmented Tasmania: the transition from Rodinia to Gondwana, Aust. J.  
696 Earth Sci., 62, 1–35, 2015.
- 697 Moore, D. H., Betts, P. G., and Hall, M.: Constraining the VanDieland microcontinent at the edge of East  
698 Gondwana, Australia, Tectonophysics, 687, 158–179, 2016.
- 699 Moresi, L., Betts, P. G., Miller, M. S., and Cayley, R. A.: Dynamics of continental accretion, Nature, 508, 245–  
700 248, 2014.
- 701 Morse, M., Gibson, G., and Mitchell, C.: Basement constraints on offshore basin architecture as determined by  
702 new aeromagnetic data acquired over Bass Strait and western margin of Tasmania, ASEG Extended  
703 Abstracts 2009, pages 1–9, <http://dx.doi.org/10.1071/ASEG2009ab042>, 2009.
- 704 Owens, T. J., Taylor, S. R., and Zandt, G.: Crustal structure at regional seismic test network stations determined  
705 from inversion of broadband teleseismic P waveforms, Bull. Seismo. Soc. Ame., 77, 631–632, 1987.
- 706 Owens, T. J. and Zandt, G.: Implications of crustal property with variations for models of Tibetan Plateau  
707 evolution, Nature, 387, 37–43, 1997.
- 708 Pan, S. Z. and Niu, F. L.: Large contrasts in crustal structure and composition between the Ordos plateau and the  
709 NE Tibetan plateau from receiver function analysis, Earth Plan. Sci. Lett., 303, 291–298, 2011.
- 710 Pilia, S., Arroucau, P., Rawlinson, N., Reading, A. M., and Cayley, R. A.: Inherited crustal deformation along

- 711 the East Gondwana margin revealed by seismic anisotropy tomography, *Geophys. Res. Lett.*, 43(23), 12082–  
712 12090, <https://doi.org/10.1002/2016GL071201>, 2016.
- 713 Pilia, S., Rawlinson, N., Cayley, R. A., Musgrave, R., Reading, A. M., Direen, N. G., and Young, M. K.:  
714 Evidence of micro-continent entrainment during crustal accretion, *Sci. Rep.*, 5,  
715 <http://dx.doi.org/10.1038/srep08218>, 2015a.
- 716 Pilia, S., Rawlinson, N., Green, N. G., Reading, A. M., Cayley, R., Pryer, L., Arroucau, P., and Duffet, M.:  
717 Linking mainland Australia and Tasmania using ambient seismic noise tomography: Implications for the  
718 tectonic evolution of the east Gondwana margin, *Gond. Res.*, 28, 1212–1227, 2015b.
- 719 Porritt, S. W. and Miller, M. S.: Updates to FuncLab, a Matlab based GUI for handling receiver functions,  
720 *Computers and Geosciences*, 111, 260–271, <https://doi.org/10.1016/j.cageo.2017.11.022>, 2018.
- 721 Rawlinson, N., Davies, D. R., and Pilia, S.: The mechanisms underpinning Cenozoic intraplate volcanism in  
722 eastern Australia, Insights from seismic tomography and geodynamic modeling, *Geophys. Res. Lett.*, 44(19),  
723 9,681–9,690, 2017.
- 724 Rawlinson, N., Housman, G. A., Collins, C. D. N., and Drummond, B. J.: New evidence of Tasmania’s tectonic  
725 history from a novel seismic experiment, *Geophys. Res. Lett.*, 28, 3337–3340, 2001.
- 726 Rawlinson, N. and Kennett, B.: Teleseismic tomography of the upper mantle beneath the southern Lachlan  
727 Orogen, Australia, *Phys. Earth Planet. Inter.*, 167, 84–97, <http://dx.doi.org/10.1016/j.pepi.2008.02.07>, 2008.
- 728 Rawlinson, N., Kennett, B., Vanacore, E., Glen, R., and Fishwick, S.: The structure of the upper mantle beneath  
729 the Delamerian and Lachlan orogens from simultaneous inversion of multiple teleseismic datasets, *Gond.*  
730 *Res.*, 19, 788–799, 2011.
- 731 Rawlinson, N., Kennett, B. L. N., Salmon, M., and Glen, R. A.: Origin of lateral heterogeneities in the upper  
732 mantle beneath Southeast Australia from seismic tomography, Khan, A., and Deschamps, F. (Eds.), *In The*  
733 *Earth’s Heterogeneous Mantle: A Geophysical, Geodynamical and Geochemical Perspective*, pages 47–78,  
734 Springer Geophysics, Springer, 2015.
- 735 Rawlinson, N., Pilia, S., Young, M., Salmon, M., and Yang, Y.: Crust and upper mantle structure beneath  
736 southeast Australia from ambient noise and teleseismic tomography, *Tectonophysics*, 689, 143–156,  
737 <http://dx.doi.org/10.1016/j.tecto.2015.11.034>, 2016.
- 738 Rawlinson, N., Pozgay, S., and Fishwick, S.: Seismic tomography: a window into deep Earth, *Phys. Earth*  
739 *Planet. Inter.*, 178, 101–135, 2010.
- 740 Rawlinson, N. and Urvoy, M.: Simultaneous inversion of active and passive source datasets for 3–D seismic  
741 structure with application to Tasmania, *Geophys. Res. Lett.*, 33, 2006.
- 742 Sambridge, M. S.: Geophysical inversion with a neighbourhood algorithm – I. Searching a parameter space,  
743 *Geophys. J. Int.*, 138, 479–494, 1999a.
- 744 Sambridge, M. S.: Geophysical inversion with a neighbourhood algorithm -II. Appraising the ensemble,  
745 *Geophys. J. Int.*, 138, 479–494, 1999b.
- 746 Saygin, E. and Kennett, B. L. N.: Ambient seismic noise tomography of Australian continent, *Tectonophysics*,  
747 481, 116–125, <http://dx.doi.org/10.1016/j.tecto.2008.11.013>, 2010.
- 748 Shibutani, T., Sambridge, M. S., and Kennett, B. L. N.: Genetic algorithm inversion for receiver functions with  
749 application to crust and uppermost mantle structure beneath Eastern Australia, *Geophys. Res. Lett.*,  
750 23, 1826–1832, 1996.
- 751 Spaggiari, C. V., Gray, D. R., and Foster, D. A.: Lachlan Orogen subduction–accretion systematics revisited,  
752 *Aust. J. of Earth Sci.*, 51, 549–553, 2004.

- 753 Spaggiari, C. V., Gray, D. R., Foster, D. A., and McKnight, S.: Evolution of the boundary between the western  
754 and central Lachlan Orogen: implications for Tasmanide tectonics, *Aust. J. Earth Sci.*, 50, 725–749, 2003.
- 755 Teasdale, J., Pryer, L., Stuart-Smith, P., Romine, K., Etheridge, M., Loutit, T., and Kyan, D.: Structural  
756 framework and basin evolution of Australia’s Southern Margin, *APPEA J. Australian Petroleum Production  
757 and Exploration Association*, 43, 13–38, <https://doi.org/10.1785/0120030123>, 2003.
- 758 Thomson, W. T.: Transmission of elastic waves through a stratified solid, *J. of App. Phys.*, 21, 89-93, 1950.
- 759 Tkalčić, H., Chen, Y., Liu, R., Huang, H., Sun, L., and Chan, W.: Multi-step modelling of teleseismic receiver  
760 functions combined with constraints from seismic tomography: Crustal structure beneath southeast China,  
761 *Geophys. J. Int.*, 187, 303–326, 2011.
- 762 Tkalčić, H., Rawlinson, N., Arroucau, P., and Kumar, A.: Multistep modelling of receiver-based seismic and  
763 ambient noise data from WOMBAT array: crustal structure beneath southeast Australia, *Geophys. J. Int.*,  
764 189, 1681–1700, <https://doi.org/10.1111/j.1365-246X.2012.05442>, 2012.
- 765 Wessel, P., Smith, W. H., Scharroo, R., Louis, J., and Wobbe, F.: Generic mapping tools: improved version  
766 released, *EOS Trans. Am. Geophys. Union*, 94, 409-420, 2013.
- 767 Young, M. K., Cayley, R. A., McLean, M. A., Rawlinson, N., Arroucau, P., and Salmon, M.: Crustal structure  
768 of the east Gondwana margin in southeast Australia revealed by transdimensional ambient seismic noise  
769 tomography, *Geophys. Res. Lett.*, 40, 4266–4271, 2013.
- 770 Young, M. K., Rawlinson, N., Arroucau, P., Reading, A., and Tkalčić, H.: High-frequency ambient noise  
771 tomography of southeast Australia: new constraints on Tasmania’s tectonic past, *Geophys. Res. Lett.*, 38,  
772 <http://dx.doi.org/10.1029/2011GL047971>, 2011.
- 773 Young, N., Tkalčić, H., Rawlinson, N., and Reading, A. M.: Full waveform moment tensor inversion in a low  
774 seismicity region using multiple teleseismic datasets and ambient noise: application to the 2007 Shark Bay,  
775 Western Australia, Earthquake. *Geophys. J. Int.*, 188,1303–1321, [https://doi.org/10.1111/j.1365-  
776 246X.2011.05326](https://doi.org/10.1111/j.1365-246X.2011.05326), 2012.
- 777 Zhu, L. and Kanamori, H.: Moho depth variation in southern California from teleseismic receiver functions, *J.*  
778 *Geophys. Res.*, 105, 2969–2980, 2000.

779

780

Table 1: Model parameter bounds used in the Neighbourhood Algorithm receiver function inversion.  $V_s^{upper}$  and  $V_s^{lower}$  represent the  $S$ -velocity at the top and bottom of a layer respectively.  $V_p/V_s$  represents  $P$  and  $S$  wave velocity ratio within a layer.

Layer	Thickness (m)	$V_s^{upper}$ (km/s)	$V_s^{lower}$ (km/s)	$V_p/V_s$
Sediment	0-2	0.5-1.5	0.5-1.5	2.00-3.00
Basement	0-3	1.8-2.8	1.8-2.8	1.65-2.00
Upper crust	3-20	3.0-3.8	3.0-3.9	1.65-1.80
Middle crust	4-20	3.4-4.3	3.4-4.4	1.65-1.80
Lower crust	5-15	3.5-4.8	3.6-4.9	1.65-1.80
Mantle	5-20	4.0-5.0	4.0-5.0	1.70-1.90

781

782

783

784

785

786

787

788

789

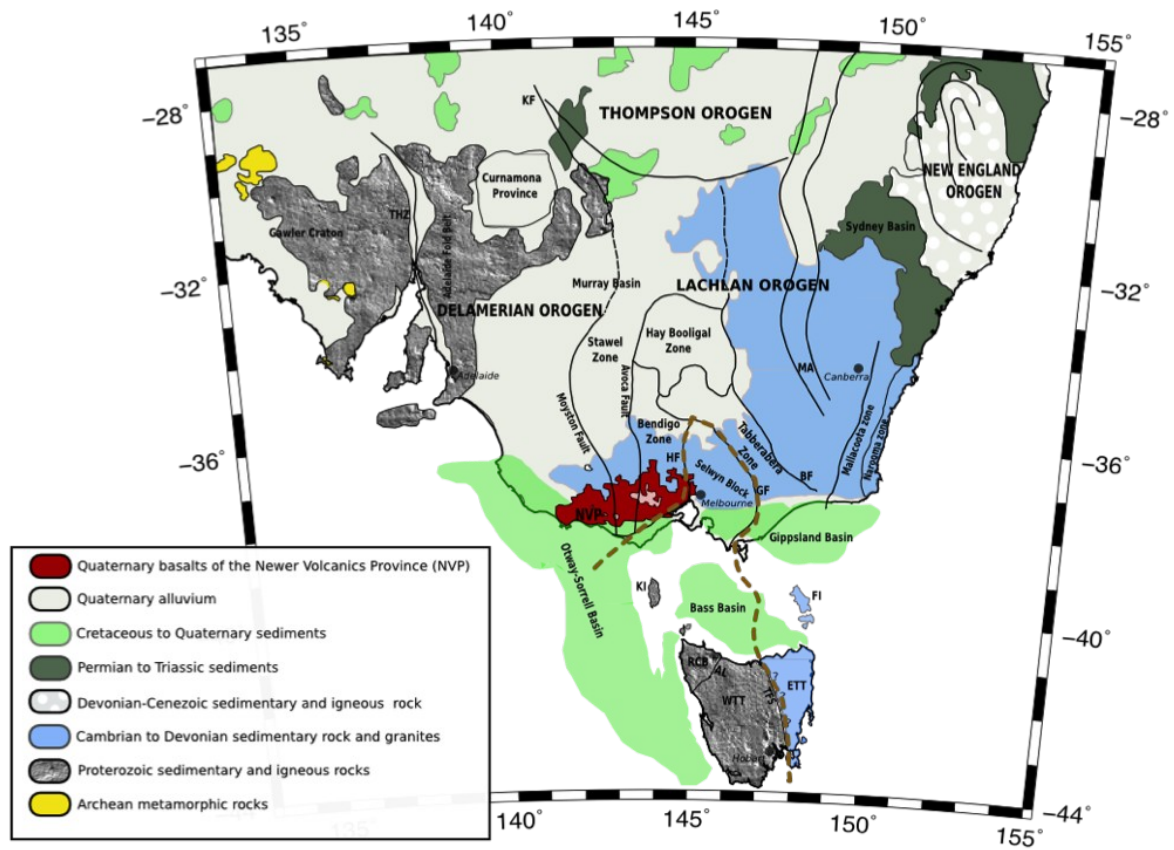
790

791

792 **Table 2:** Summary of H- $\kappa$  stacking and NA inversion results for the current study.

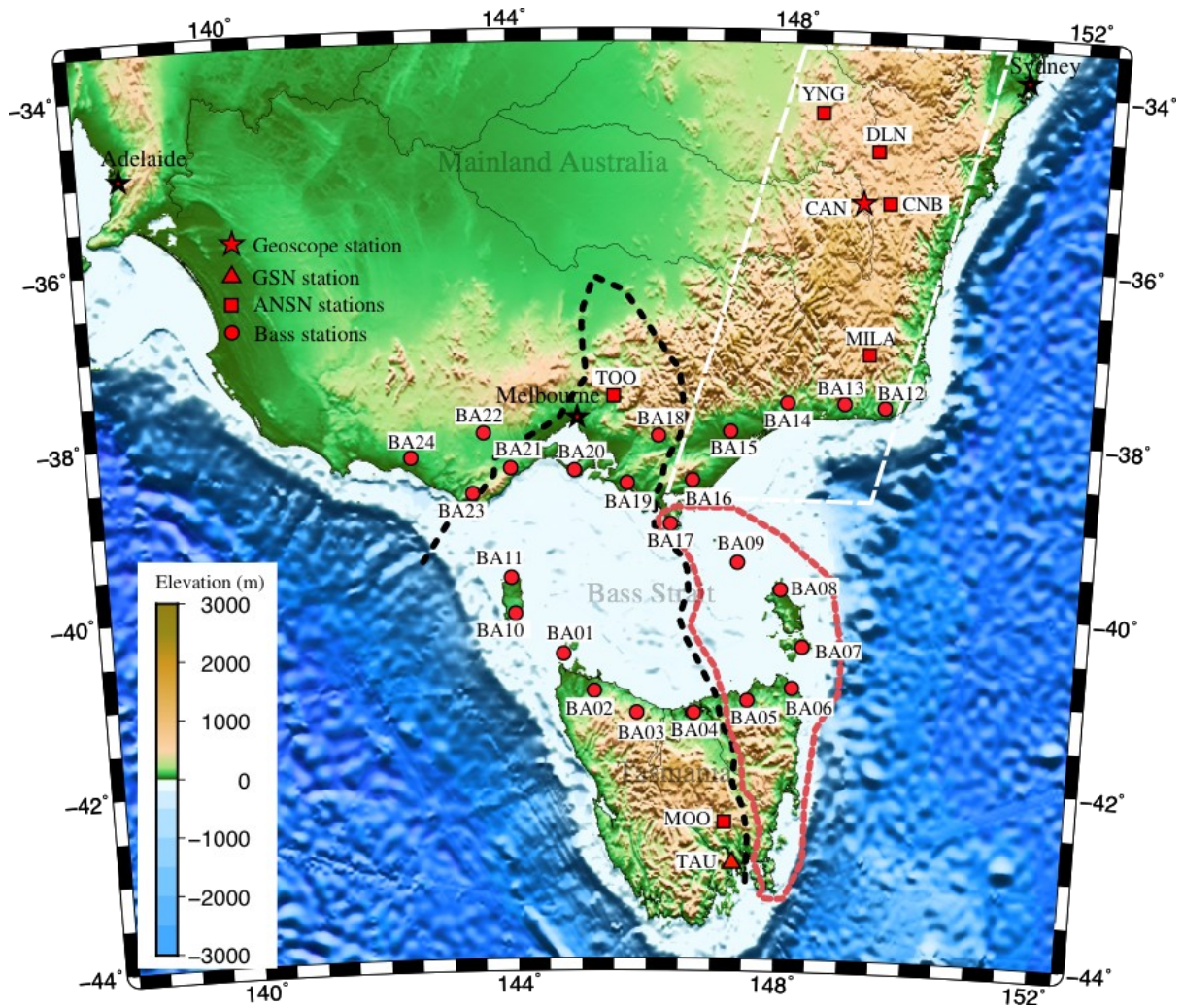
Basic station information					Results				
Type	Station name	Lon (°)	Lat (°)	No of RFs	Moho Depth (km) (H-K stacking)	Bulk $V_p/V_s$ (H-K stacking)	Moho Depth (km) (NA inversion)	Quality (NA inversion)	Moho type (NA inversion)
Temporary stations	BA02	145.20	-40.95	9	23.2±5.0	1.83±0.31	-	Moderate	Not evident
	BA03	145.84	-41.20	8	-	-	-	Moderate	Not evident
	BA07	148.31	-40.43	6	32.5±0.1	1.70±0.02	28	Good	Sharp
	BA08	147.97	-39.77	8	31.9±0.1	1.70±0.07	-	Poor	-
	BA09	147.32	-39.47	8	32.8±1.7	1.71±0.07	32	Good	Sharp
	BA11	143.98	-39.64	12	30.5±2.1	1.65±0.07	-	-	-
	BA13	148.83	-37.63	24	37.7±2.9	1.74±0.10	40	Good	Sharp
	BA17	146.33	-39.04	20	30.9±2.5	1.76±0.10	29	Good	Broad
	BA18	146.14	-38.02	3	-	-	38	Good	Sharp
	BA19	145.69	-38.57	20	25.5±2.4	1.93±0.14	-	Good	Not evident
	BA20	144.92	-38.42	30	26.3±1.6	1.93±0.12	29	Good	Sharp
	BA22	143.61	-37.99	5	-	-	29	Poor	Sharp
BA24	142.54	-38.26	4	-	-	33	Poor	Sharp	
Permanent stations	TAU	147.32	-42.91	41	33.5±1.9	1.70±0.08	33	Poor	Intermediate
	MOO	147.19	-42.44	58	33.0±1.2	1.71±0.04	34	Good	Sharp
	TOO	145.59	-37.57	276	37.5±1.2	1.68±0.04	36	Good	Sharp
	YNG	148.40	-34.20	178	37.3±0.5	1.76±0.04	35	Good	Sharp
	CAN	149.00	-35.32	402	39.1±0.5	1.73±0.02	40	Good	Sharp
	CNB	149.36	-35.32	155	38.5±1.1	1.70±0.04	39	Good	Broad
	MILA	149.16	-37.05	4	37.6±2.1	1.73±0.06	-	-	-

793  
 794  
 795  
 796  
 797



799 **Figure 1: Regional map of southeastern Australia that shows key geological boundaries and the location of observed**  
 800 **or inferred tectonic units (modified from Bello et al., 2019a). Thick black lines delineate structural boundaries and**  
 801 **the thick brown dashed line traces out the boundary of Van Dieland. HF = Heathcote Fault; GF = Governor Fault; BF**  
 802 **= Botheragandra Fault; KF = Koonenberry Fault; THZ = Torrens Hinge Zone; MA = Macquarie Arc, NVP =**  
 803 **Newer Volcanics Province;; KI = King Island and FI = Flinders Island in Bass Strait; WTT = West Tasmania**  
 804 **Terrane; ETT = East Tasmania Terrane; AL = Arthur Lineament; TFS = Tamar Fracture System and RCB = Rocky**  
 805 **Cape Block. Outcrop boundaries are sourced from Rawlinson et al. 2016.**

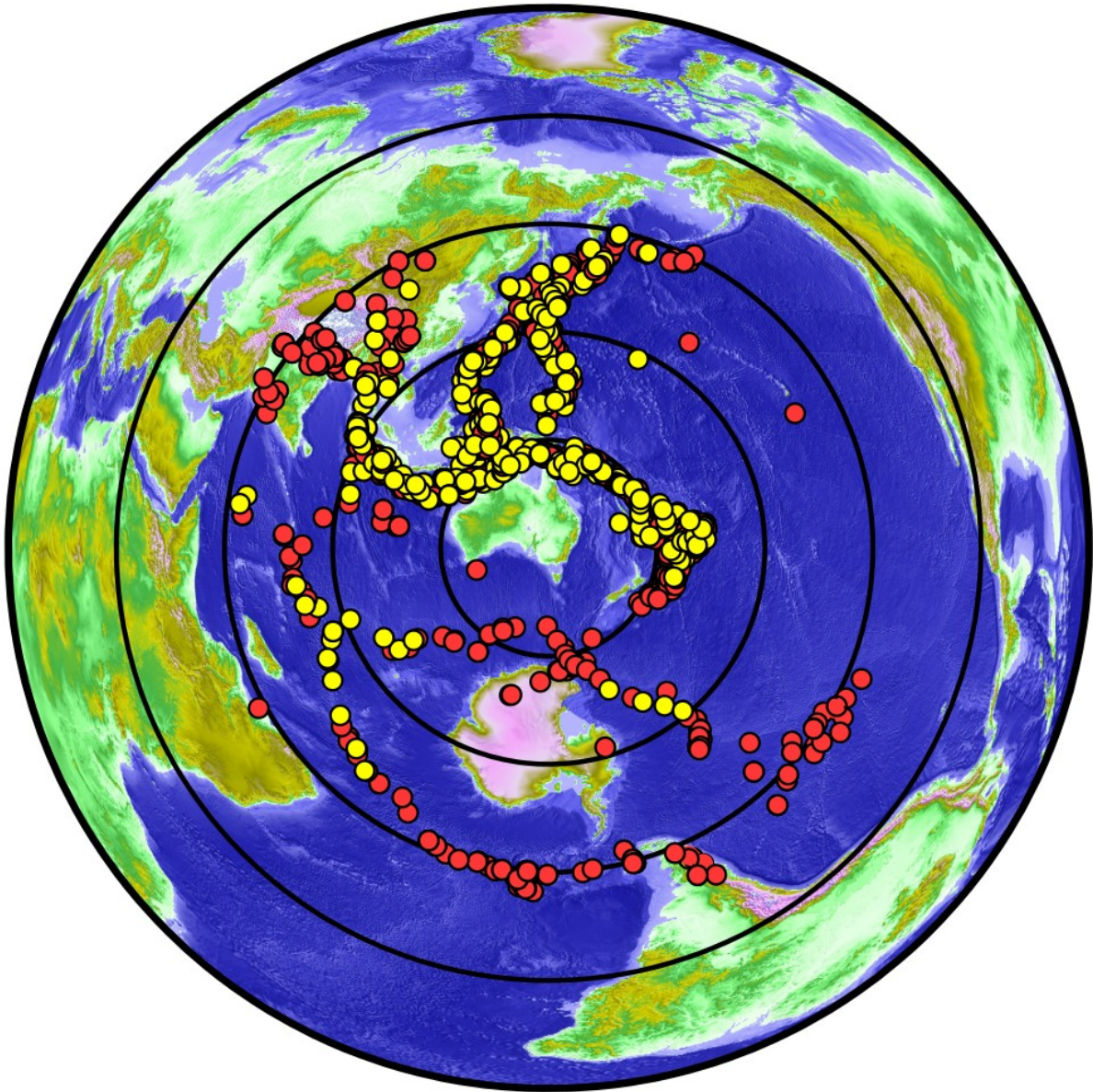
806  
 807  
 808



811 **Figure 2: Location of seismic stations used in this study superimposed on a topographic/bathymetric map of**  
 812 **southeast Australia (modified from Bello et al., 2019a). The boundary of VanDieland is delineated by a thick**  
 813 **black dashed line. Thick red dashed line outlines the boundary of the East Tasmania Terrane and Furneaux**  
 814 **Islands. Thick white dashed line highlights the eastern sector of the Lachlan Fold Belt.**  
 815 **Topography/bathymetry is based on the ETOPO1 dataset (Amante and Eakins, 2009).**

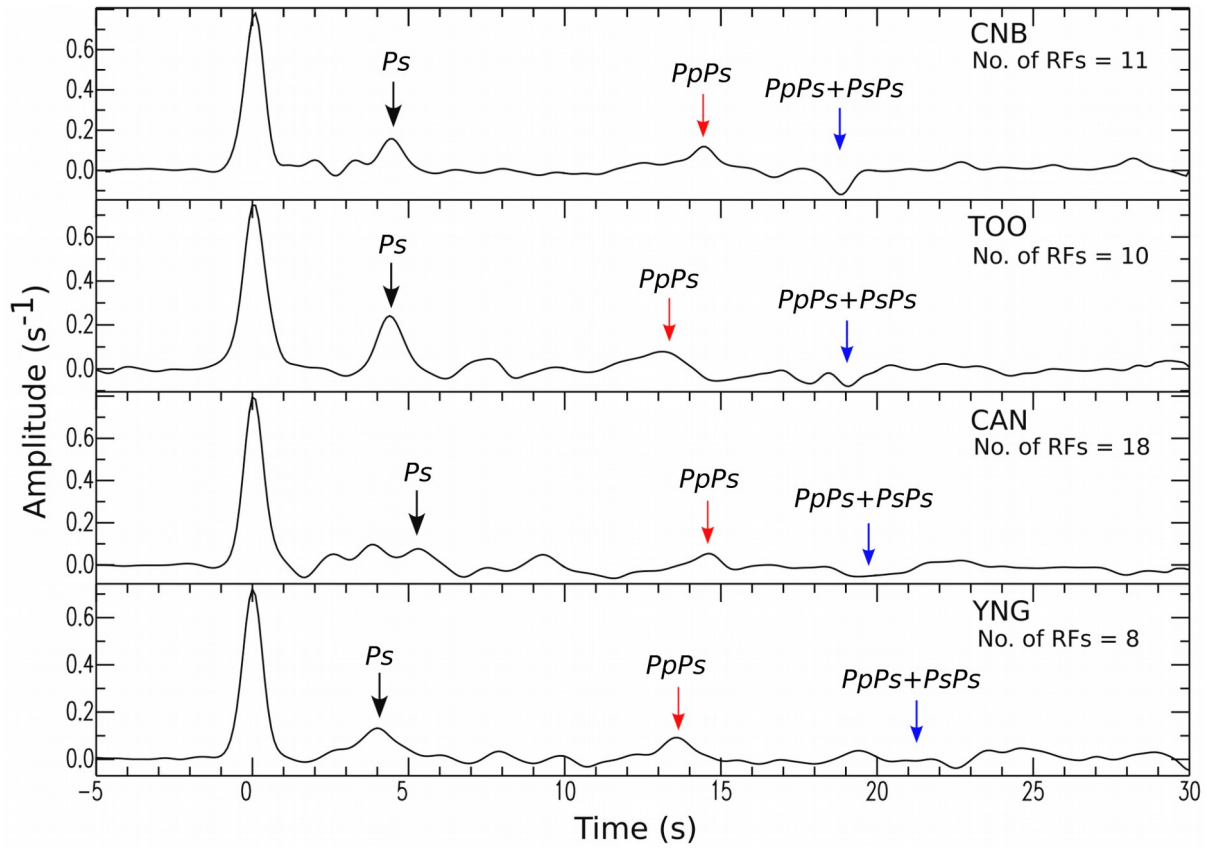
816

817  
818



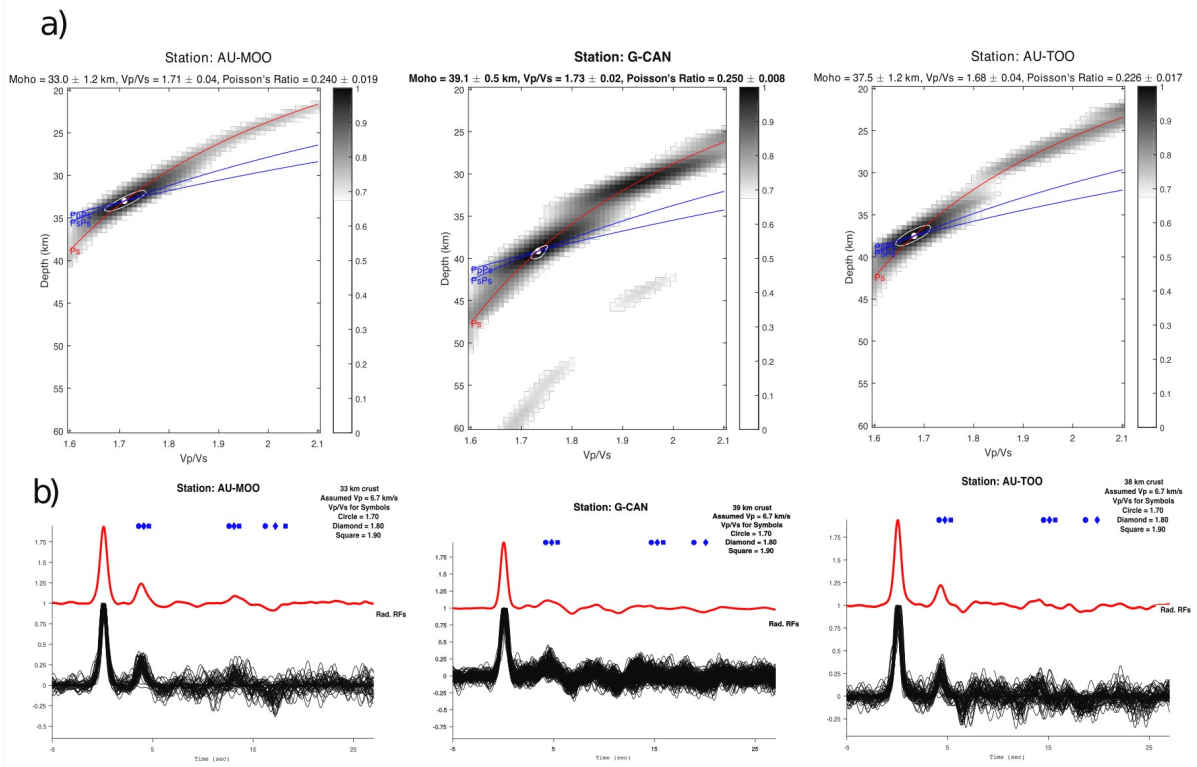
820 Figure 3: Distribution of distant earthquakes (teleseisms) used in this study. The locations of events that are  
821 ultimately used for RF analysis are denoted by yellow dots. Concentric circles are plotted at 30° intervals from the  
822 centre of Bass Strait. Topography/bathymetry colours are based on the Etopo1 dataset (Amante and Eakins, 2009).

823



825 **Figure 4: Stacked receiver functions from Australian National Seismic Network (ANSN) stations TOO, YNG, MOO**  
 826 **and GSN station TAU. Small arrows indicate arrival of the  $P_s$  (black),  $PpPs$  (red) and  $PpPs + PsPs$  (blue) phases from**  
 827 **the Moho.**

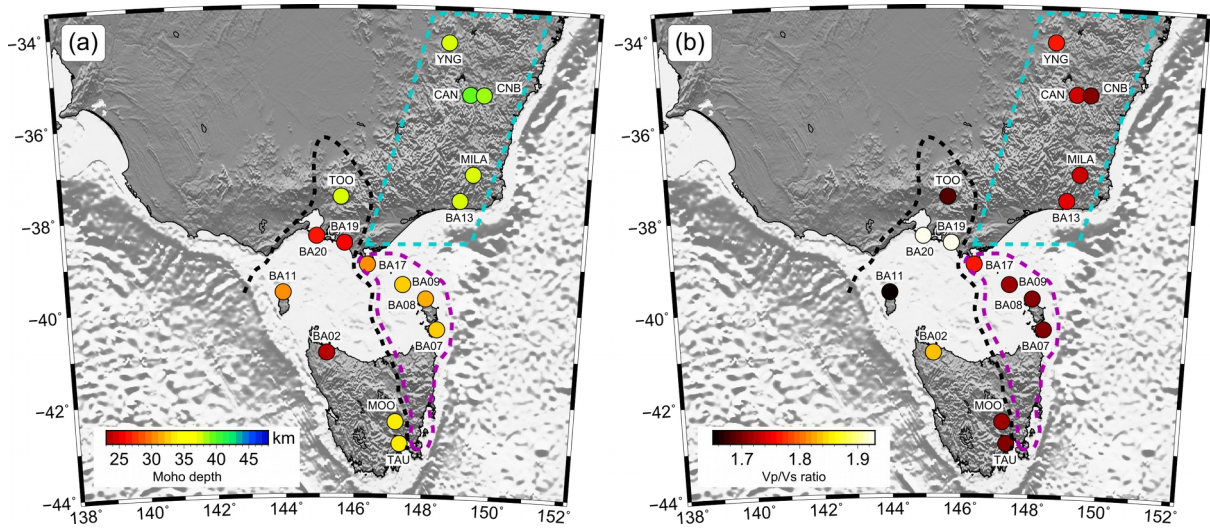
828  
829  
830



832 **Figure 5: Results from the  $H-\kappa$  stacking analysis for RFs (Zhu and Kanamori, 2000) at stations MOO, CAN and**  
833 **TOO. In each case (a) normalised amplitudes of the stack over all back-azimuths along the travel time curves**  
834 **corresponding to the  $P_s$  and  $P_pP_s$  phases. (b) Corresponding stacked receiver function for each station.**

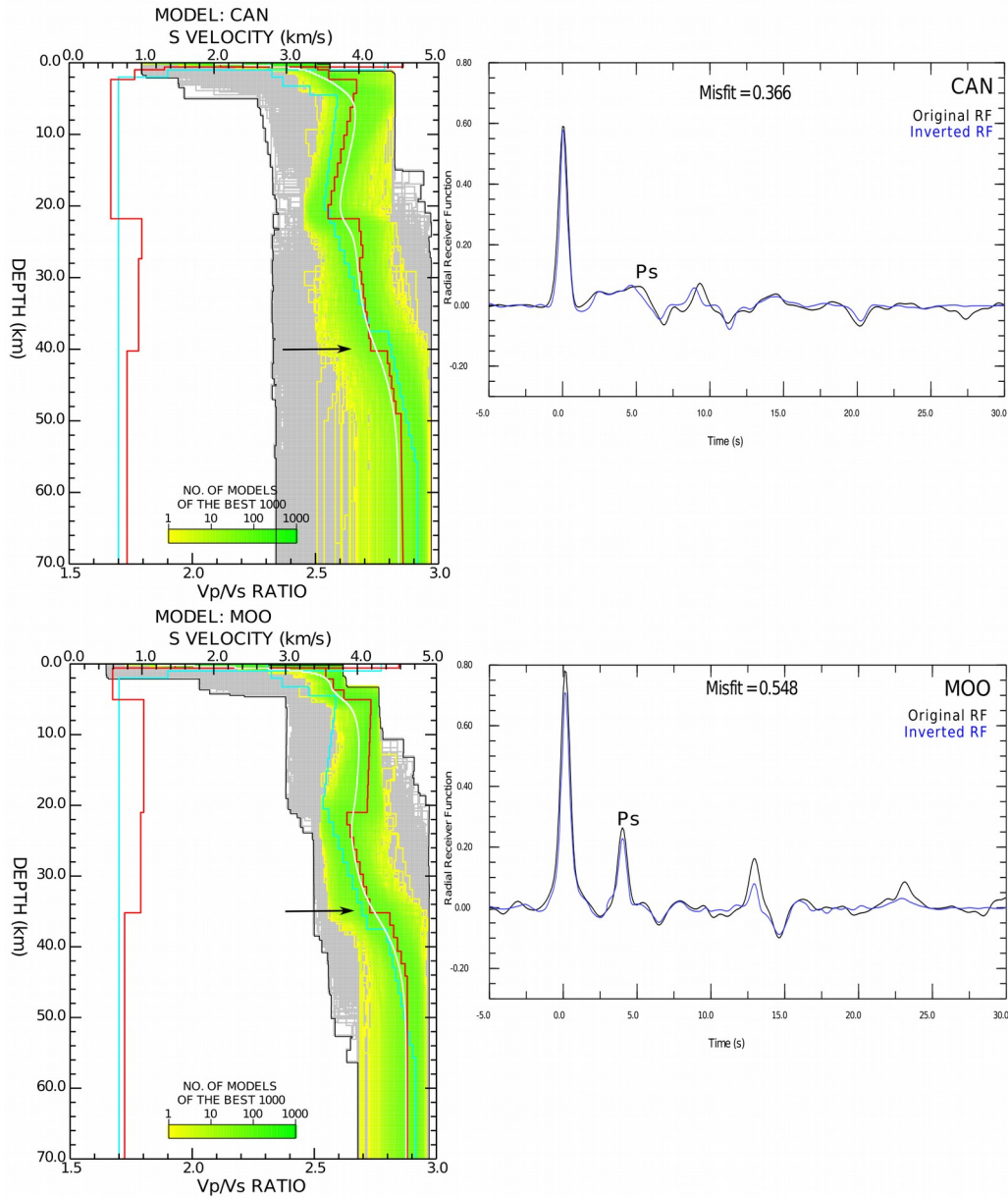
835

836



838 Figure 6: (a) Variations in crustal thickness and (b)  $V_p/V_s$  ratio taken from the linear ( $H-\kappa$ ) stacking results (Table 2).  
839 Crustal thickness varies between  $\sim 23$  and 39 km.  $V_p/V_s$  ratios vary from  $\sim 1.65$  to 1.93. Thick black dashed line  
840 denotes the boundary of VanDieland. Thick magenta dashed line outlines the boundary of East Tasmania Terrane  
841 and eastern Bass Strait (ETT+EB). Thick cyan dashed line highlights the eastern part of the Lachlan Fold Belt.  
842 Illuminated topography/bathymetry is based on the Etopo1 dataset (Amante and Eakins, 2009).

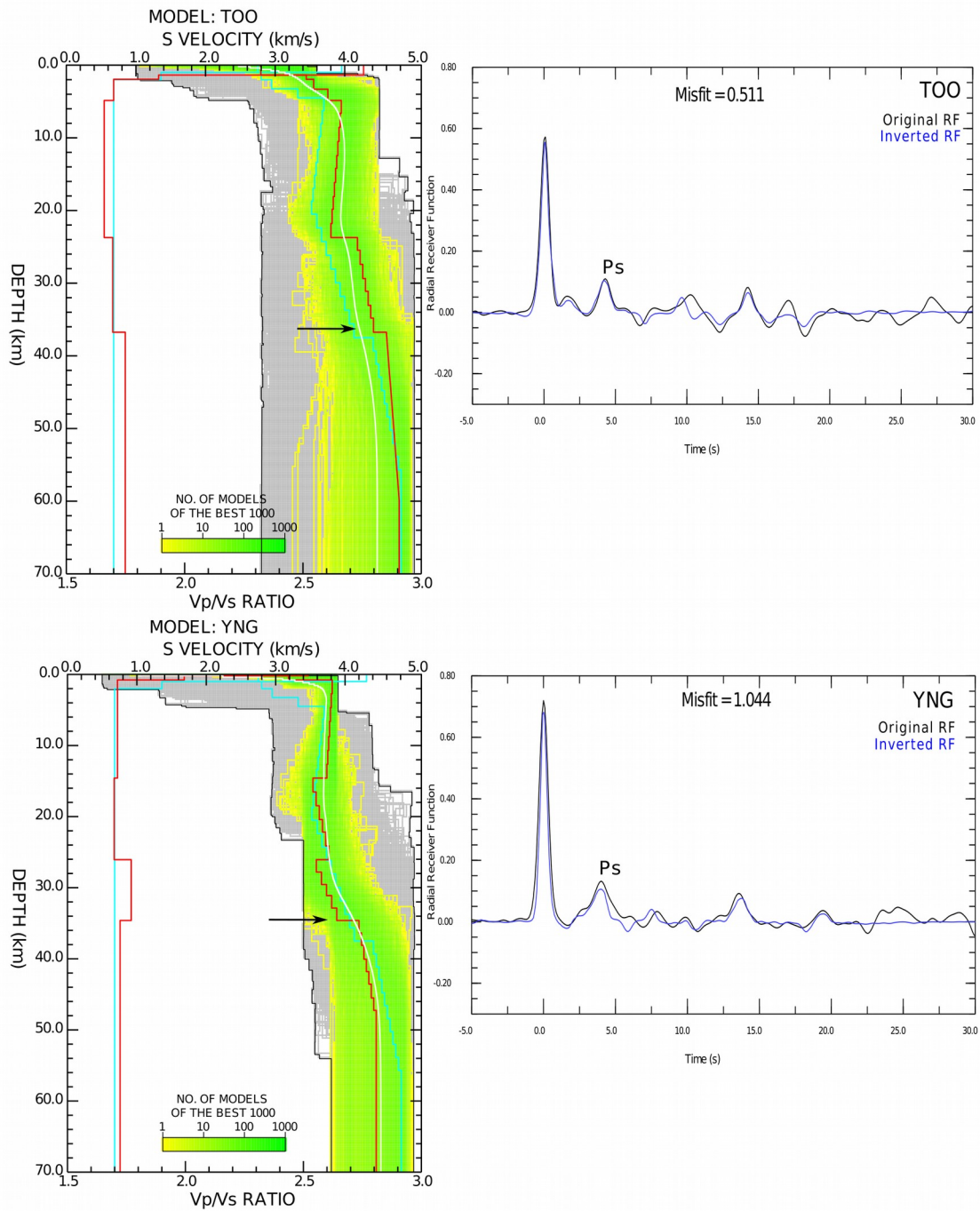
843  
844



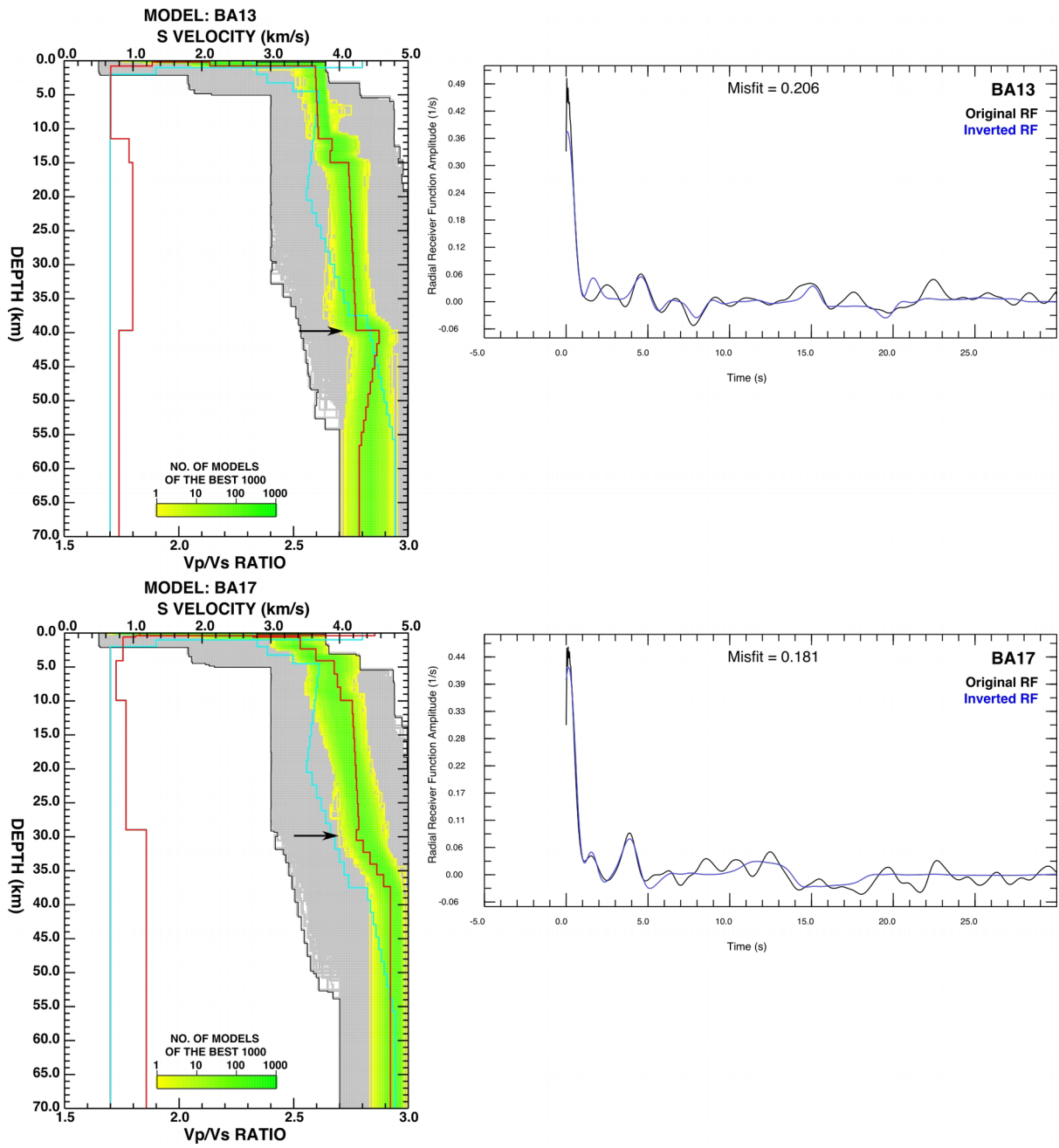
846 **Figure 7: (Left) Seismic velocity models for CAN and MOO stations obtained from the neighbourhood algorithm**  
847 **(Sambridge 1999a). The grey area indicates all the models searched by the algorithm. The best 1000 models are**  
848 **indicated by the yellow to green colours; the best one (smallest misfit) corresponds to the red line, both for  $S$ -wave**  
849 **velocity (top horizontal axis) and  $V_p/V_s$  ratio (bottom horizontal axis) and the white line is the average velocity model.**  
850 **Small black arrows denote the estimated depth of the Moho. (Right) Waveform matches between the observed**  
851 **stacked receiver functions (black) and predictions (blue) based on the best models. “Misfit” refers to the chi-square**  
852 **estimate as defined by Equation 2.**

853  
854

855  
856

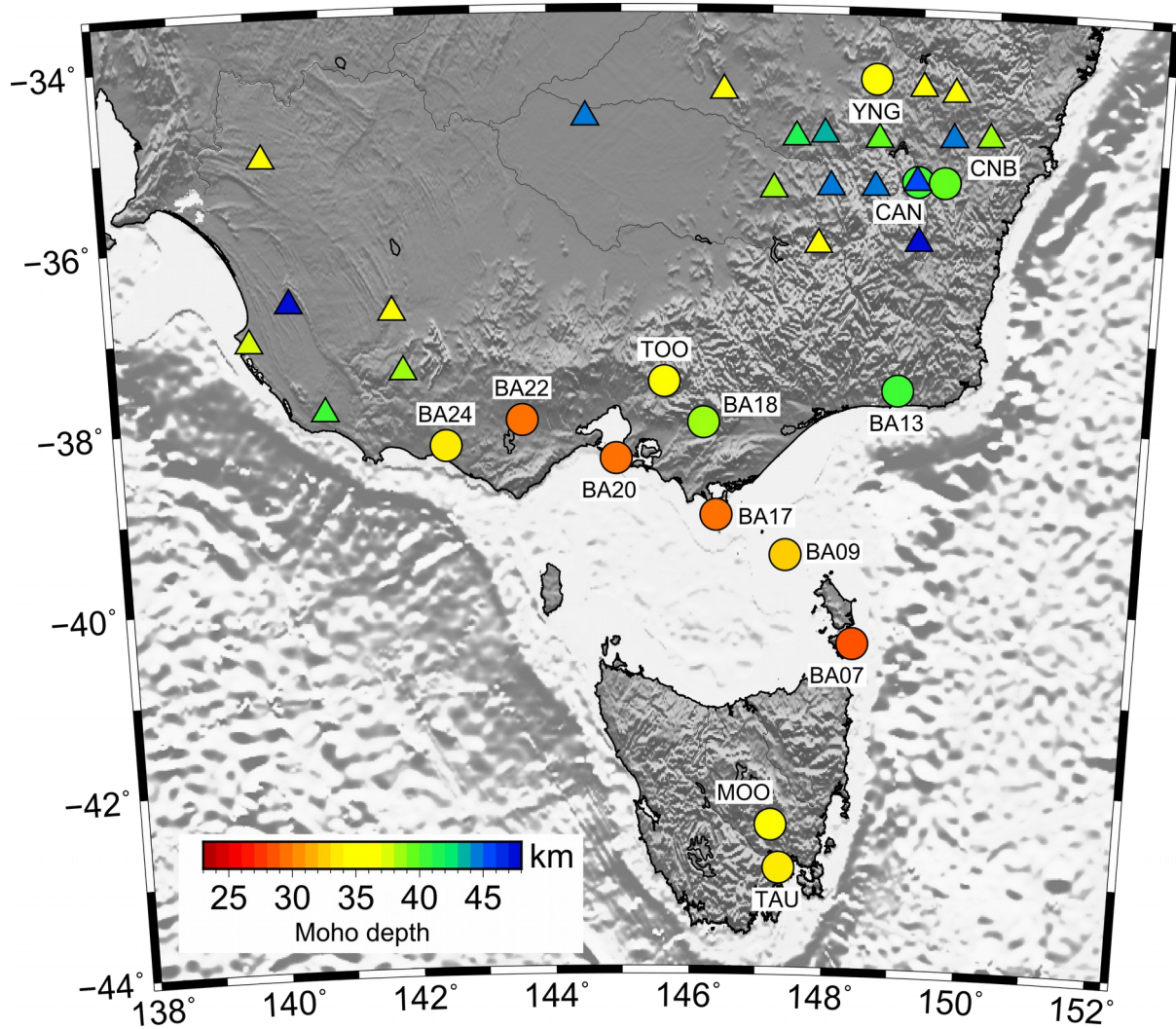


857 **Figure 8: (Left) Seismic velocity models for stations TOO and YNG obtained from the neighbourhood algorithm.**  
858 **(Right) Comparison between the observed stacked and the predicted receiver functions from the NA inversion. See**  
859 **Figure 7 caption for more details.**



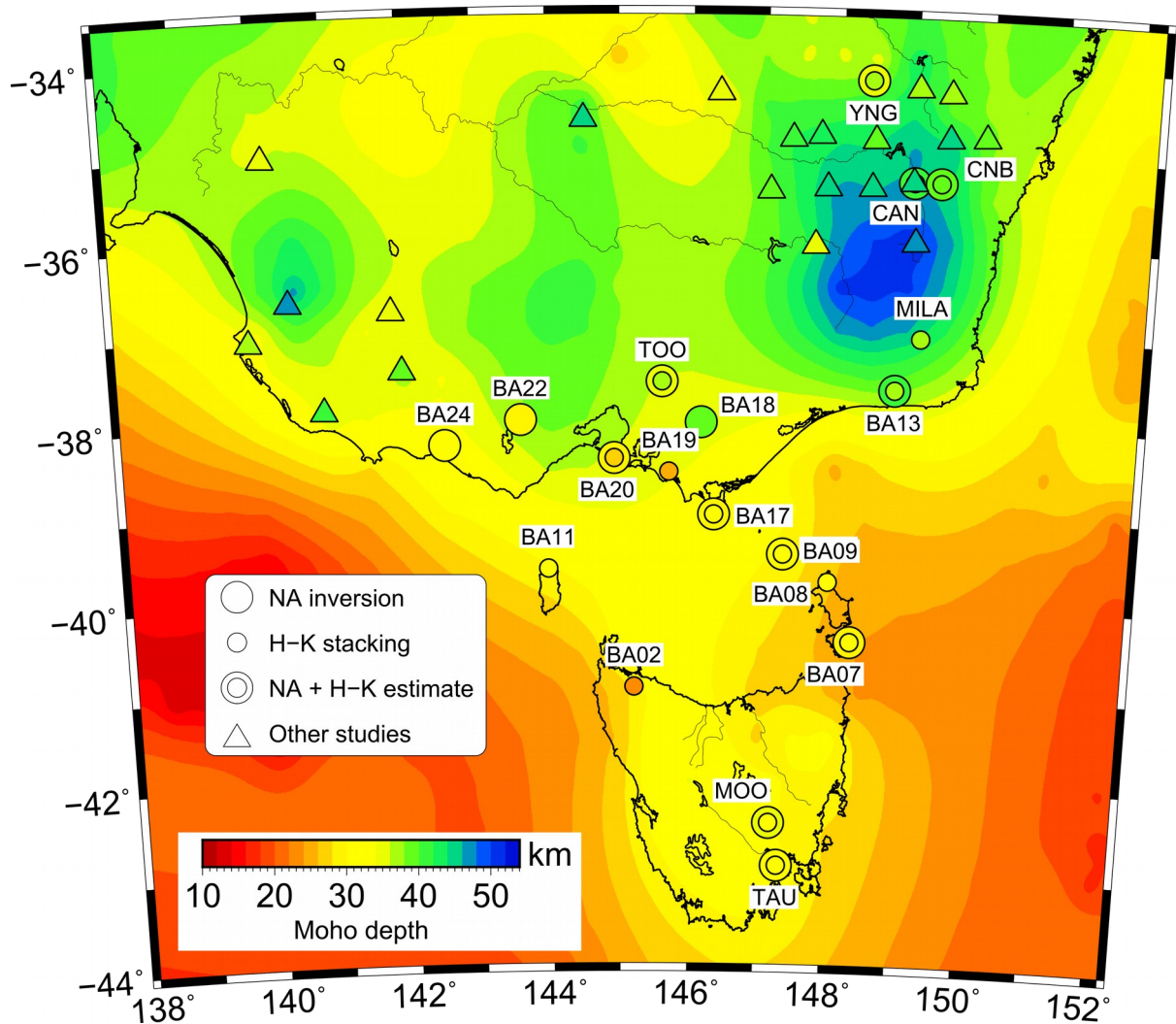
862 Figure 9: (Left) Seismic velocity models for temporary stations BA13 and BA17 obtained from the neighbourhood  
 863 algorithm. (Right) Comparison between the observed stacked and the predicted receiver functions from the NA  
 864 inversion. See Figure 7 caption for more details.

865  
866  
867  
868  
869



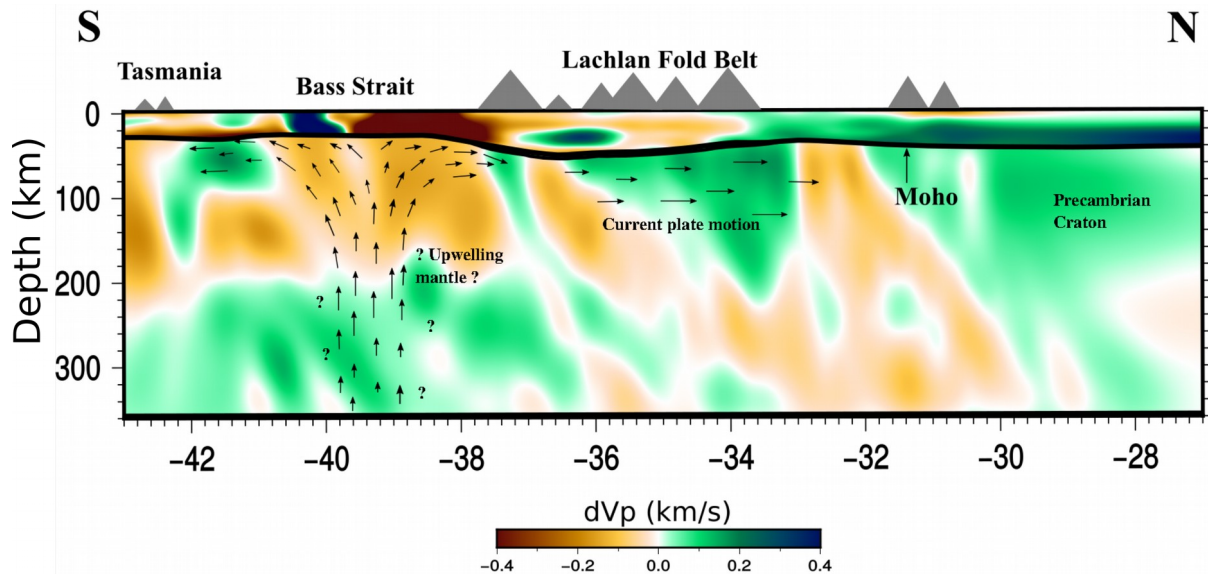
871 **Figure 10:** Map showing crustal thickness variations based on the S-wave velocity inversion results of this study  
872 (circles) and previous studies (triangles) (Clitheroe et al., 2000, Fontaine et al., 2013a,b; Shibutani, 1996; Tkalcić et al,  
873 2013). Topography/bathymetry is based on the Etopo1 dataset (Amante and Eakins, 2009).

874



877 **Figure 11: Comparison between the AusMoho model (background colour map) and Moho depths determined**  
 878 **through RF analysis in this and previous studies. Small coloured circles denote the Moho depths determined from**  
 879 **H- $\kappa$  stacking, whereas large coloured circles correspond to receiver function estimates. When both H- $\kappa$  and NA-**  
 880 **derived depths are available at a single station, the smaller H- $\kappa$  circle is superimposed on the larger NA-**  
 881 **both depths can be observed on the one plot. Moho depths determined from previous RF studies are denoted by**  
 882 **triangles.**

883



886 Figure 12: Composite result of teleseismic tomography (mantle velocity anomalies), ambient noise (crustal velocity  
 887 anomalies), receiver functions (Moho) and shear wave splitting (inferred mantle flow relative to over-riding plate).  
 888 Velocity slices are taken at 148°E. Note that the the crustal model produced from ambient noise tomography is  
 889 defined in terms of  $V_{sv}$ , but was converted to  $V_p$  in the study of Bello et al. (2019b) to permit its inclusion in the  
 890 starting model for the inversion of teleseismic P-wave arrival time residuals. In this figure, the crustal  $V_p$  anomalies  
 891 are shown.

892

893

894